Wing Tip Vortex Dependence with Angle of Attack

David May

A Thesis

in

The Department

of

Mechanical and Industrial Engineering

Presented in Partial Fulfillment of the Requirements
for the Degree of Master of Applied Science (Mechanical Engineering) at
Concordia University
Montreal, Quebec, Canada

August 2005

Your file Votre référence
ISBN: 0-494-14311-8
Our file Notre référence
ISBN: 0-494-14311-8

Abstract

Wing Tip Vortex Dependence with Angle of Attack

David May

This study examines Wing Tip Vortex flows, in the Near to Far Field. A Viscous Incompressible simulation of the NACA 0012 (with an aspect ratio of 6, operating at a free stream Reynolds number of $6.84e5$) was made. This simulation used the Spalart-Allmaras Turbulence Model combined with Wall Functions. Wing performance characteristics, of Lift and Drag Coefficients, as calculated numerically are compared with the values as obtained by Prandl conventional Lifting Line Method together with the airfoil section data; the difference in Lift and Drag coefficients between the methods is obtained.

The Tip vortex parameters are compared with available, current, experimental data. Once the validity of the model is assessed, the fluid structures and dynamical processes are described, with the aid of solution visualizations. Characteristics of the flow that have not been studied in open literature are presented.

An analysis is conducted regarding the dependence of the Tip Vortex characteristics and their variation with Angle of Attack. Aspects of the, low wing loading, analysis of Moore and Saffman are summarized and assumed to apply in the Far Field Regime. Then, dimensional analysis is used to present reasonable arguments for the

scaling of the observed Near Field data. A balance of these two scaling laws is made and is shown to apply in what will be called the Intermediate Field Regime, where dependence with various vortex characteristics display a logarithmic variation with Angle of Attack.

Table of Contents

List of Figures

List of Tables

1 Introduction

The fundamental methodology in the design of a lifting surface is that if fluid elements on the upper surface travel relatively faster than those of the lower surface, then lift will be generated. It is well known that, if the fluid far outside the wing boundary layer is irrotational, then Bernoullis equation at one point near the upper surface and another near the lower surface will result in a pressure difference. Via Boundary Layer Theory, the pressure in these regions may be used to approximate the pressure directly on the wall that is responsible for lifting the surface. For a high aspect ratio (very long) wing, the pressure distribution at any spanwise station should be identical, but for the fluid in the vicinity of the wing tip, there is an inherent three-dimensionality to the flow. In this region the flow senses the pressure gradient, as imposed by the center portion of the wing, and as a result, there is a secondary component of flow in the direction of this gradient.

Certain aspects of this secondary flow may be immediately obtained. The gradient in velocity, as created by the wing, and for the most part concentrated in the boundary layer, is conveniently quantified with the use of vorticity and, its integrated value, circulation. Due to Helmholtz, and his inescapable conclusion that vorticity is divergence free (it is to be noted that this is a kinematic property independent of fluid or flow), we understand that total, integrated, vorticity generated in the wake is, necessarily, equal to that bound to the lifting surface. We note that, not all the vorticity is in the streamwise direction, however, far enough from the wing most of it will be. Of course, energy is required to

sustain the motion of the wake; this energy is supplied by the lifting body and is felt by it as a major component of its drag. This drag component is a necessary evil, as is clear from our discussion, and is implied in its name "the drag due to lift".

Expressing vorticity as a material quantity is useful; it allows us to understand why as the particles move, the vorticity attached to them induce an additional convection on the flow field. This interaction creates the tendency for vorticity to concentrate and to generate a swirling motion in the flow. This well known behavior is observed in the mixing layers (or shear layers) of jets, as created by buoyancy or otherwise. This flow manifestation, that is responsible for concentration of the vorticity, is known in technical jargon as the rolling up of the vortex sheet and as it rolls-up it creates an ever more tightly wound spiral. Finally, fluid friction due to viscosity, gives this sheet a finite thickness and allows it to form two completely coherent vortices of opposite rotational direction. Eventually, the two vortices distance themselves from the wing, as a result, the tangential velocity profile has no external geometry to scale with and so it becomes self-similar and axisymmetric. These vortices are often quite strong, particularly in the case of heavily loaded wings, and have a tendency to induce a downward motion on each other. Meanwhile, they will consistently decay, smearing their vorticity over the flow field, reducing the magnitudes of their velocity, until some other mechanism, of stochastic nature, causes them to be no longer identifiable.

This is the basic underlying process, however, there are many details to this process, which are yet to be fully understood. It is the aim of this thesis to take us further into the tip vortex by identifying some of its underlying mechanics.

2 Computational Setup

The computational component of this study was conducted using a commercially available CFD software package, FLUENT version 6.1.22. These computations were carried out on a single PC that contained a Pentium 4, 2.80 GHz processor and 2 Gb of RAM. FLUENT uses the discretized control volume technique to calculate the fluxes of various quantities through the domain. The meshed domain allows these integral equations to be turned into equivalent algebraic systems that are then solved numerically. This is achieved by applying the governing equations to the individual cells that compose the computational domain; the last yields discrete equations that conserve each quantity over the cell. FLUENT is a tool and this is the method in which it was used, only minor attention was put into modifying parameters that affect the discretization; the objective of the numerical work was to gain inspiration and insight into the physical processes that are occurring. Table 1 summarizes the various options chosen in formulating the discretization and model flow.

Table 1: Solver Settings

Settings	
Solver Type	
Precision	*Single*
Solver	*Segregated, implicit formulation*
Space	*3D*
Gradient option	*Cell based*
Time	*Steady*
Discretization	
Pressure	*Second-Order*
Momentum	*Second-Order Upwind*
Pressure-Velocity Coupling	*SIMPLE*
Modified Turbulent Viscosity	*First-Order Upwind*
Flow Model	
Energy	*No*
Viscous	*Spalart-Almaras, Strain-Vorticity Based Production*
Density	*Constant*
Molecular Viscosity	*Constant*

2.1 Reynolds-Averaged Navier-Stokes and Turbulence Model

The equations being approximated are continuity and the incompressible Reynolds averaged Navier-Stokes. Using indicial notation, these are,

$$\frac{\partial \overline{u}_i}{\partial x_i} = 0$$

$$\frac{D\overline{u}_i}{Dt} = -\frac{1}{\rho}\frac{\partial p}{\partial x_i} + \nu \frac{\partial \overline{u}_i}{\partial x_j \partial x_j} - \frac{\partial}{\partial x_j}\left(\overline{u'_i u'_j}\right)$$

Where u_i is the i^{th} component of velocity, x_i is the i^{th} spacial component, p is the pressure and ν is the kinematic viscosity. When a variable has an overbar it indicates its mean value and when it has an apostrophe it indicates its variable component, such that $u = \overline{u} + u'$. The turbulence model used in the present study was the Spalart-Allmaras model [1]. The model has terms that modify the turbulent viscosity based on the production, destruction, amplifying and damping at the wall.

2.1.1 Turbulence Modeling

The significance of the turbulent viscosity is based on the Boussinesq approximation; this approximation states that,

$$-\rho\overline{u_i' u_j'} = \mu_t\left(\frac{\partial \overline{u_i}}{\partial x_j} + \frac{\partial \overline{u_j}}{\partial x_i}\right) - \frac{2}{3}\left(\rho k + \mu_t \frac{\partial \overline{u_i}}{\partial x_i}\right)$$

however in the Spalart-Allmaras model the second term is simply neglected so that we may express the Reynolds stresses by,

$$-\rho\overline{u_i' u_j'} = \mu_t\left(\frac{\partial \overline{u_i}}{\partial x_j} + \frac{\partial \overline{u_j}}{\partial x_i}\right)$$

Where ρ is the density, and μ_t is the turbulent viscosity. The Boussinesq assumption immediately models the turbulence as being an isotropic quantity that affects the flow in a fashion similar to that of viscosity, namely, the effect of the turbulence is to diffuse the momentum. Note that the Boussinesq approximation achieves nothing to the effect of closing the system of equations, it simply allows for the modeling a more physically meaniful quantity, the turbulent viscosity, rather than tackling the Reynolds stresses directly. Closure of the system is the objective of the Spallart-Allmaras model.

The Spalart-Allmaras Model is a one-equation model that achieves closure empirically for the turbulent (eddy or effective) viscosity. It does this directly, without solving for length scales, in a manner, which was inspired by the Baldwin-Barth model. Also, just like Baldwin-Barth it is popular in the aerospace industry, probably because of its relative simplicity and moderate success in modeling many useful flows.

The transport equation for the Spalart-Allmaras model is,

$$\frac{\partial}{\partial t}(\rho\tilde{\nu})+\frac{\partial}{\partial x_i}(\rho\tilde{\nu}u_i)=G_\nu+\frac{1}{\sigma_{\tilde{\nu}}}\left[\frac{\partial}{\partial x_j}(\mu+\rho\tilde{\nu})\frac{\partial\tilde{\nu}}{\partial x_j}+C_{b2}\rho\left(\frac{\partial\tilde{\nu}}{\partial x_j}\right)^2\right]-Y_\nu$$

Defining the following values,

$$x=\left(\frac{\tilde{\nu}}{\nu}\right), f_{v1}=\left(\frac{x^3}{x^3+{C_{v1}}^3}\right), f_{v2}=1-\left(\frac{x}{1+xf_{v1}}\right), \tilde{S}=S+\frac{\tilde{\nu}}{\kappa^2 d^2}f_{v2}$$

The turbulent viscosity is then obtained from,

$$\mu_t = \rho \tilde{\nu} f_{v1}$$

The turbulent viscosity production is obtained from,

$$G_v = C_{b1} \rho \tilde{S} \tilde{\nu}$$

where C_{b1} and κ are constants, d is the distance from the wall, and S is a scalar value which is a function of the deformation tensor. In FLUENT two options are given for calculating this value of S. First option is the one originally proposed and it is calculated as,

$$S = \sqrt{2 \Omega_{ij} \Omega_{ij}}$$

where,

$$\Omega_{ij} = \frac{1}{2}\left(\frac{\partial u_i}{\partial x_j} - \frac{\partial u_j}{\partial x_i}\right)$$

We see that only near the walls is the production of turbulence a function of the vorticity, whereas further from the wall this functional relationship decreases.

A modification of this function, proposed by Dacles-Mariani et al. [2] during a study of tip vortices in the near field proposed the following,

$$S = \sqrt{2\Omega_{ij}\Omega_{ij}} + C_{prod} \min\left(0, \sqrt{2S_{ij}S_{ij}} - \sqrt{2\Omega_{ij}\Omega_{ij}}\right)$$

with the mean strain rate, S_{ij}, defined as

$$S_{ij} = \frac{1}{2}\left(\frac{\partial u_i}{\partial x_j} + \frac{\partial u_j}{\partial x_i}\right)$$

Doing this has the direct effect of reducing the production of turbulent viscosity in regions were the measure of vorticity is greater than the measure of strain. Such a case is encountered in the viscous core of a tip vortex, where it has been noted that turbulence is damped in this region of near solid body rotation, and thus low strain. It was for this very reason that the modification was proposed and as a result has been tailored to this specific case. Because of this, it was decided to use this option in the present study.

Defining the following quantities,

$$f_w = g\left(\frac{1+C_{w3}^6}{g^6 + C_{w3}^6}\right)^{1/6}, g = r + C_{w2}\left(r^6 - r\right), r = \frac{\tilde{\nu}}{S\kappa^2 d^2}$$

The destruction term is modeled as,

$$Y_\nu = C_{w1}\rho f_w\left(\frac{\tilde{\nu}}{d}\right)^2$$

The constants were calibrated based on the values that are observed in many of the common aerodynamic flows seen in the aerospace industry; the model is not by any means universal but is well tailored to the problem that we are interested. The constants have the following default values,

$$C_{b1} = 0.1355, C_{b2} = 0.622, \sigma_{\tilde{\nu}} = 2/3, C_{v1} = 7.1,$$
$$C_{w1} = \frac{C_{b1}}{k^2} + \frac{1+C_{b2}}{\sigma_{\tilde{\nu}}}, C_{w2} = 0.3, C_{w3} = 2, \kappa = 0.4187$$

These values were used in the present study.

2.1.2 Wall Modeling

Although not originally included in the model, FLUENT has implemented the turbulence model to incorporate wall functions so that mesh does not need to be as fine in, viscous affected, wall regions. This is done in anticipation that the sublayer need not be resolved to achieve a reasonable approximate solution.

Complete resolution of the boundary layer, near the wall, requires a relatively large number of cells. This becomes increasingly impractical as the Reynolds number of the flow is increased. A well-established, semi-empirical, alternative is to use modeling of the wall effects.

When the mesh is fine enough to resolve the laminar sublayer, the wall shear stress is obtained from the laminar stress-strain relationship:

$$\frac{u}{u_\tau} = \frac{\rho u_\tau y}{\mu} = y^+$$

Where u is the velocity parallel to the wall, $u_\tau = \sqrt{\frac{\tau_w}{\rho}}$ the square root of the wall shear stress divided by the density and is called the shear velocity, y is the distance from the

wall and μ is the viscosity. If the mesh is too coarse to resolve the laminar sublayer, it is assumed that the centroid of the wall-adjacent cell falls within the logarithmic region of the boundary layer, and the law-of-the-wall is employed:

$$\frac{u}{u_\tau} = \frac{1}{\kappa}\ln\left(E\frac{\rho u_\tau y}{\mu}\right) = \frac{1}{\kappa}\ln\left(Ey^+\right)$$

κ is the von Kármán constant (0.4187), and $E = 9.7393$

It is shown, in Figure 2-1, that the test case under study has values of wing $y^+ < 200$ at all locations on the wing. This is safely within the logarithmic region from the point of view of turbulent boundary layers on a flat plate with an applied pressure gradient.

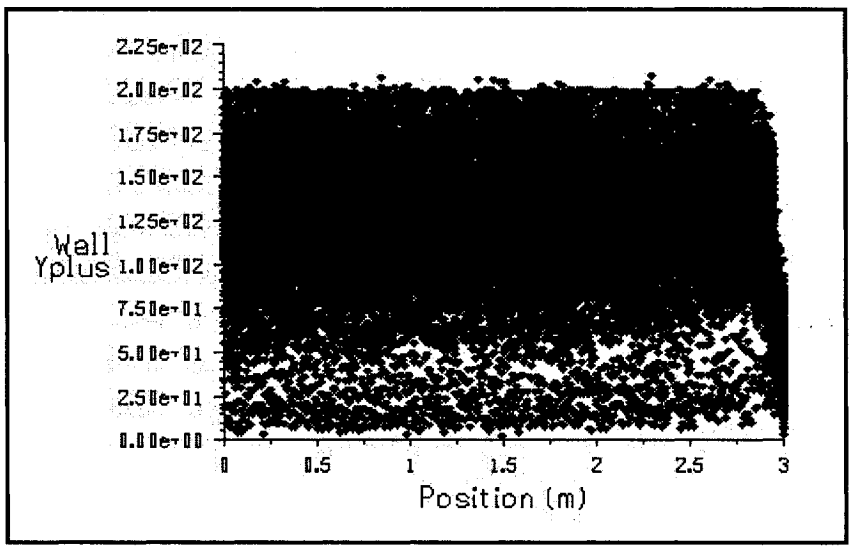

Figure 2-1: Wall Y^+

2.2 The Meshed Computational Domain

A three-dimensional unstructured tetrahedral mesh was used, several screen shots depicting the general character of the mesh are displayed in Figure 2-2, Figure 2-3,

Figure 2-4, Figure 2-5. The choice of the tetrahedral mesh was made based on the objective of capturing the three-dimensional nature of the tip vortex. The mesh constructed originally has 1817521 cells and 317122 nodes but is subsequently put through a single adaption to eliminate the outlier values of y^+.

A computational domain that approximated the effects of an external flow was needed. On the rational basis that the main geometry affecting the structure of the tip vortex must be the characteristics of the tip itself, it was suspected that the computational domain would not need to be especially large to preserve this structure (Another testament to this is the size of many of the wind tunnels used in Near Field tip vortex experiments [2], [3], [4], [5] and the computational domains of other tip vortex studies [6], [7], [8], [9],[10]). It was finally decided that the domain would be 30 chords in length, 20 chords in width and 10 chords in height; this is on the safe side, however, the mesh in much of the far region is very coarse. Additionally, it could be argued that it was also desirable to reduce the effect of the approximate boundary conditions. The wing had a half span of 3 chords and was placed five chords from the inlet. Since the computational domain was very large, and since most of the gradients are in the vicinity of the wing and in its wake, size functions had to be used in the mesh to ensure efficient computation. Particular care was taken in the location near the tip to ensure accurate prediction of the flow structure in this vicinity; at the tip the cells were given a start size of 0.0046 chords. Also the size functions were used near the leading and trailing edge to capture the gradients. After sufficient initial convergence was achieved a single adaption on the values of y^+ was undertaken, doing this ensured a $y^+ < 200$, which is safely expected to lie in the overlap

region, and therefore the Law of the Wall is, expected to be, a valid approximation. We can also note from the figure that the y^+ in the vicinity of the wing tip is on average lower than that on the rest of the wing.

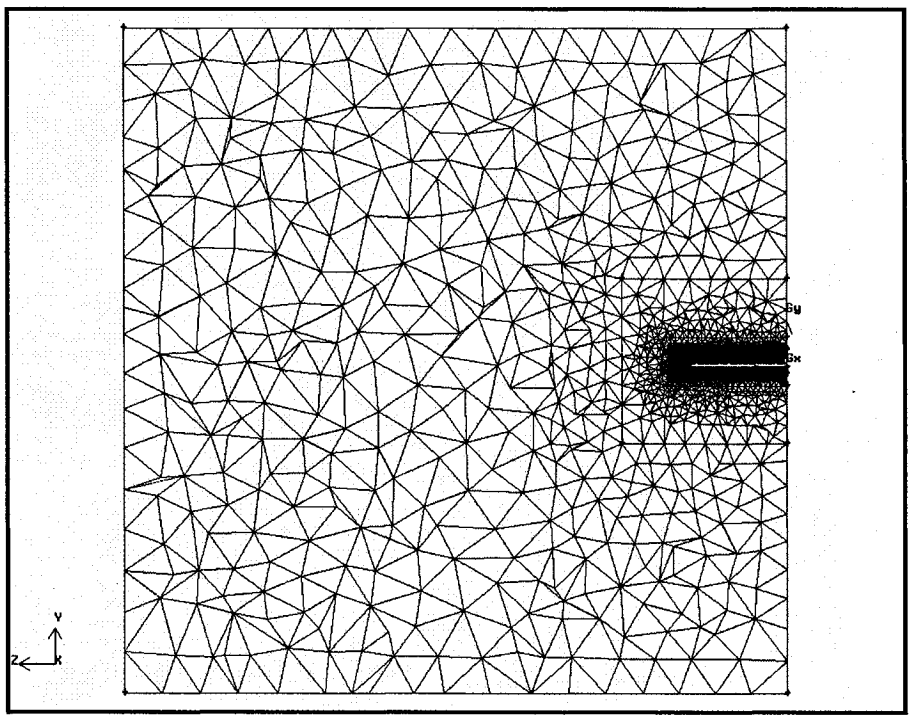

Figure 2-2: Mesh Section 1

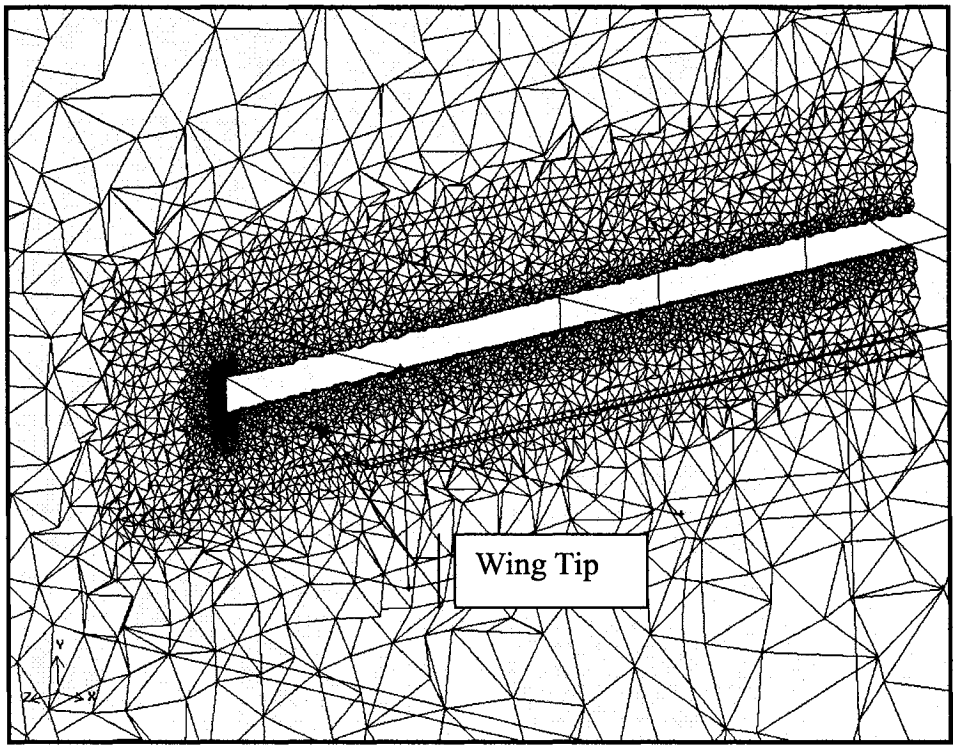

Figure 2-3: Mesh Section 2

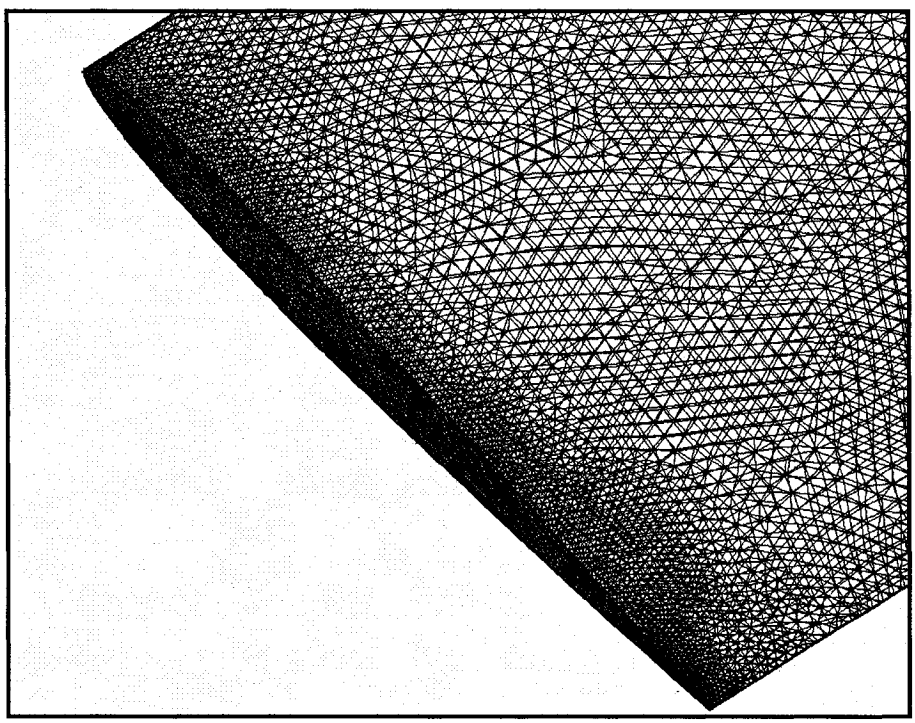

Figure 2-4: Mesh Section 3

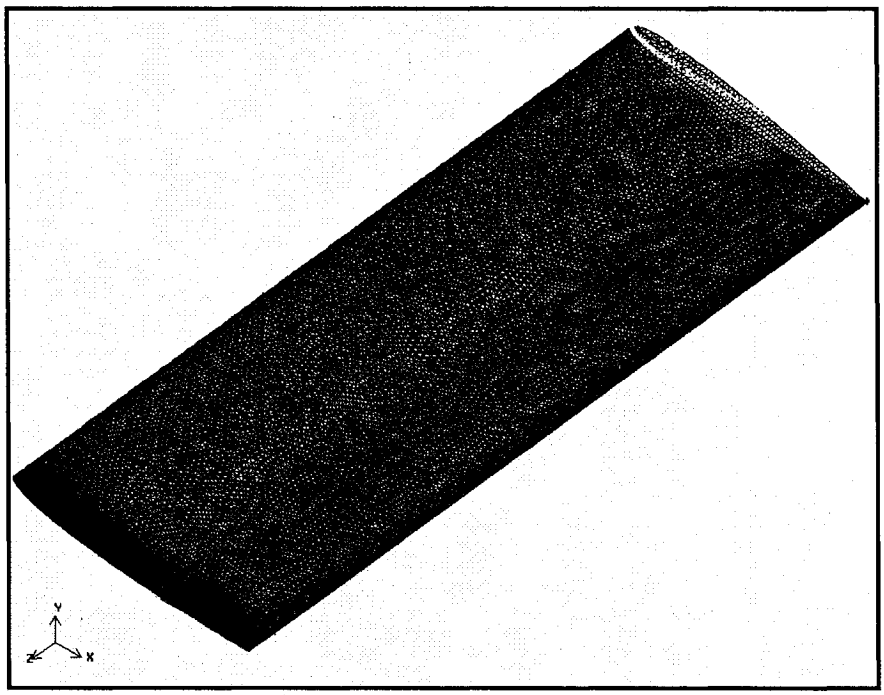

Figure 2-5: Mesh Section 4

2.3 Boundary Conditions

The application Boundary Conditions in FLUENT is a trivial matter. At the inlet to the domain a uniform velocity, $10\,m/s$ was given, its value in turn fixed the Reynolds number, since the fluid is assumed to be air. The exit condition was simply given the reference pressure, $0kPa$ so that the value of pressure throughout the domain would now be offset based on the exit value. The no penetration and no slip conditions were imposed on the wing such that velocity normal and tangential to the surface was eliminated. The surface, that the wing was fixed to, was given a symmetry boundary condition, such that variation of all quantities perpendicular to this surface is zero. The extents of the computational domain, shown in Figure 2-6, far away from the wing, were given a value of zero shear stress at the wall, in other words, the fluid was allowed to slip along the

surface but only motion tangent to this surface was permitted. It is to be observed that, this is actually mathematically equivalent to the symmetry boundary condition. These boundary conditions are summarized in Table 2.

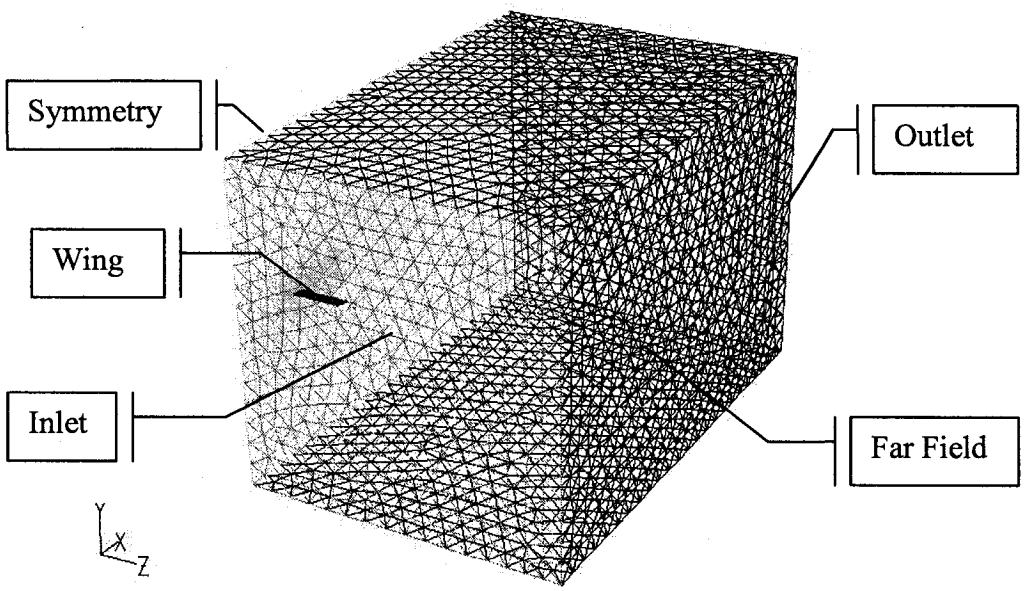

Figure 2-6: Computational Domain

Table 2: Boundary Conditions

Surface	Boundary Conditions
Wing	*Wall*
Inlet	*Velocity Inlet*
Outlet	*Pressure Outlet*
Far Field	*No Shear, Wall*
Symmetry	*Symmetry*

2.4 Convergence

Convergence was monitored by looking at the values of the residuals (see Table 3) as well as monitoring values of Lift Coefficient, Drag Coefficient, and Moment Coefficient. Because of the large computational domain, where for the most part the flow was uniform, residuals were required to reach very low values before convergence was obtained for any coefficient. As a result of this, the criterion for convergence was that the residuals be decreasing monotonically and that all three coefficients have converged. The validity of the Lift coefficient and Drag Coefficient (it is observed that the moment coefficient is quite low) are assessed in what follows. Their values are in Table 4,

Table 3: Residual Values

Residual	Value
Continuity	*4.45E-07*
x-velocity	*3.60E-08*
y-velocity	*1.31E-08*
z-velocity	*1.21E-08*
Turbulent Viscosity	*3.95E-08*

Table 4: Wing Performance, Obtained in Fluent

Coefficient	Value
Lift	*0.705553*
Drag	*0.061936*
Moment	*0.007547*

This is a convenient time to comment on the choice of tetrahedral mesh, and its difficulty to conform to the true wing shape. Its effect is to create light roughness on the surface of the wing, particularly on the leading edge, as can be seen in Figure 2-7. Recall, the objective is to be able to resolve the tip vortex, this being said, the choice of mesh was a foreseeable and justifiable trade-off.

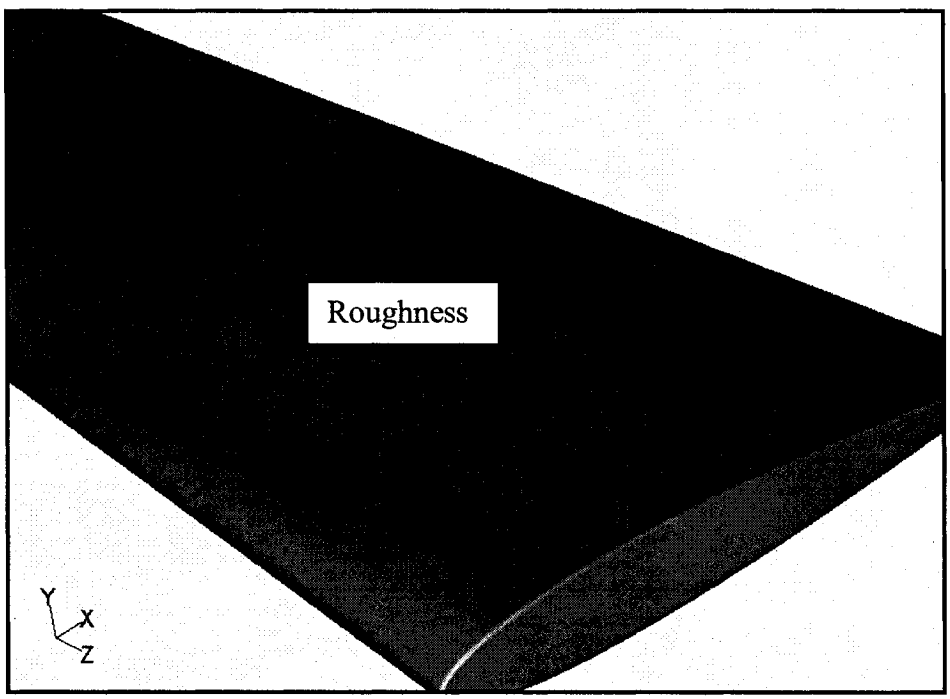

Figure 2-7: Wing, Depicting Roughness

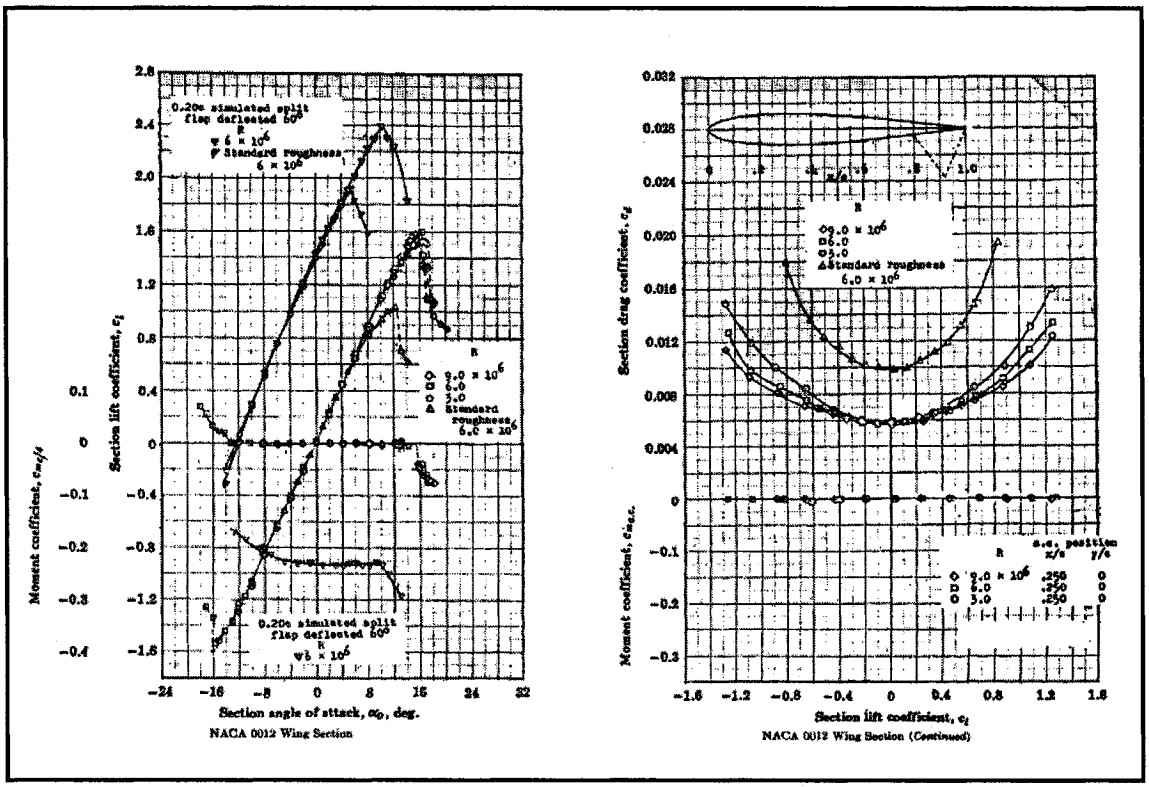

Figure 2-8: Airfoil Section Data [11]

We may obtain a reasonable approximation to the true value of C_L using conventional PLLT (Prandl Lifting Line Theory). It is shown, in Figure 2-8, that the two dimensional lift slope is given by,

$$a_0 \cong 2\pi$$

Using this, we may now solve the Lifting Line equation, using the Collocation Method as outlined by Bertin in his classic textbook on Aerodynamics[12]. That is, for the case of a rectangular wing, this equation takes on the form,

$$\left(\frac{a_0}{AR}\frac{\pi}{2}\right)\alpha \sin\phi_i = \sum_{n=1}^{N} A_{2n-1} \sin\left((2n-1)\phi_i\right)\left(\left(\frac{a_0}{AR}\frac{\pi}{2}\right)(2n-1)+\sin\phi_i\right)$$

written for $i = 1....N$

Where $\frac{y}{s} = -\cos\phi$ varying between is a transformation fixing the spanwise position. AR is the aspect ratio and α is the (geometric) angle of attack. This equation is a statement that the lift is contributed to by, a geometric angle of attack, as well as, an induced angle of attack, resulting from the downwash. We evaluate this equation at N spanwise positions defined by,

$$\phi_i = \frac{\pi}{2}\left(\frac{i}{N}\right) \text{ written for } i = 1....N$$

We then obtain a system of N, such that we may solve for the unknown coefficients A_n. Once we have done this we may solve for the lift loading using,

$$\frac{C_l}{C_L} = \left(\frac{2}{A_1\pi}\right)\sum_{n=1}^{N} A_{2n-1}\sin\left((2n-1)\phi\right)$$

Where C_l is the sectional lift and C_L is the lift of the wing. Below, in Figure 2-9, contains the lift distribution as calculated by this simple method. The various curves correspond to $N = 1,2,3 \& 7$. It is shown that we have spatial convergence for the Load Distribution even at $N = 3$.

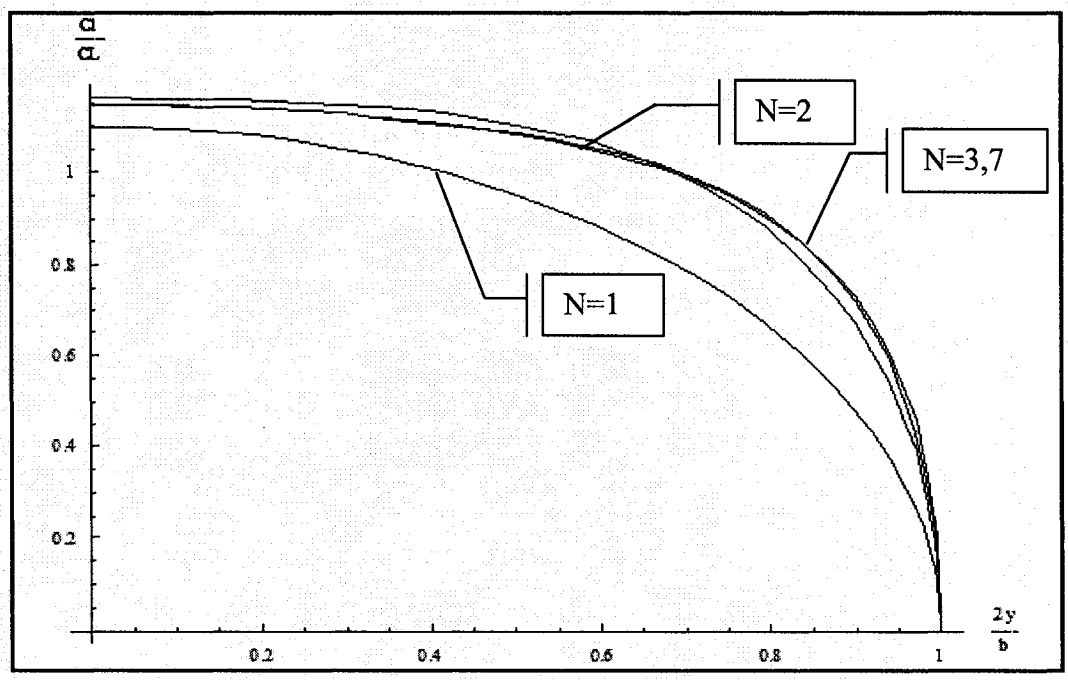

Figure 2-9: Span Loading Distribution, from PLLT Collocation Method, for various levels of truncation, N=1,2,3,7

This loading distribution, as obtained by the PLLT method, can be compared to the one that was achieved in the numerical simulation, as is shown in Figure 2-10. This was done by dividing the half span into equal sections and integrating the lifting component of the pressure on each individual section to obtain the local lift coefficient, corresponding to its spanwise location.

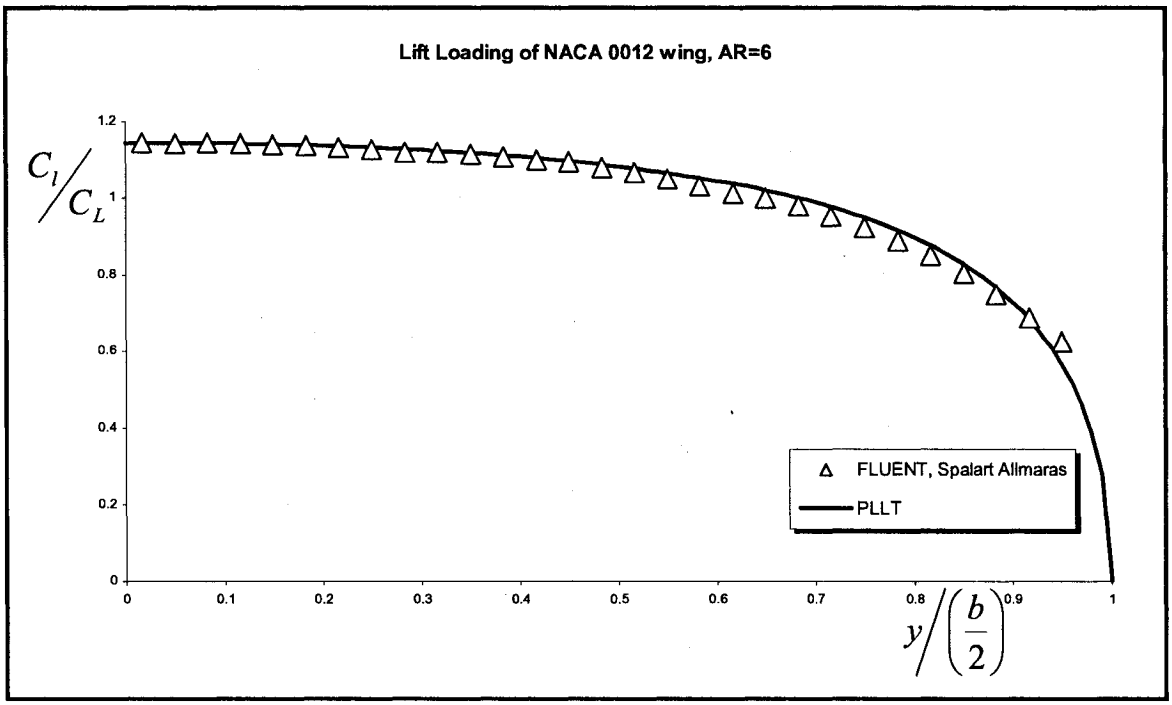

Figure 2-10: Comparison of the Lift Loading

The value of lift as calculated by this method is given by,

$$C_L = A_1 \pi (AR)$$

The lift as calculated by the PLLT collocation method, for these values of N is,

Table 5: PLLT Lift Coefficient

N	A_1	C_L
1	*0.036149*	*0.681393*
2	*0.041434*	*0.781013*
3	*0.041832*	*0.788515*
7	*0.041926*	*0.790286*

Which shows convergence for of the Lift Coefficient.

When comparing this with the Lift Coefficient as obtained from FLUENT this yields a difference of

$$C_L\,difference \cong \left\| \frac{0.79 - 0.71}{0.71} \right\| 100\ \% = 10.1\%$$

This is within the acceptable difference, for the prediction of lift of a three dimensional wing, considering the approximate means of calculation and the effect of the roughness on the leading edge. When looking at the two dimensional lift curve we see that there could be a possible departure from linearity for this particular case.

We can use the PLLT method along with the airfoil section data to approximate the value of the Drag Coefficient. This is done using,

$$C_d = C_{d,i} + c_d$$

Where c_d corresponds the two dimensional profile drag of the aerofoil section. $C_{d,i}$ is the drag induced by the downwash. c_d, using Figure 2-8, is approximately (we have to extrapolate slightly because the curve does not extend that far),

$$c_d \cong 0.021$$

Next, we calculate the induced drag from the PLLT collocation method using the expression,

$$C_{d,i} = \frac{C_L^{\,2}(1+\delta)}{AR\pi}$$

Where,

$$\delta = \sum_{n=2}^{N} (2n-1)\frac{A_{2n-1}^{\,2}}{A_1^{\,2}}$$

The relevant values for calculating this quantity are displayed in Table 6,

Table 6: PLLT Coefficient Values

n	A_{2n-1}	$(2n-1)A_{2n-1}^2/A_1^2$
1	*0.0419256*	*1*
2	*0.0050992*	*0.044377*
3	*0.0010787*	*0.00331*
4	*0.00030514*	*0.000371*
5	*0.00010508*	*5.65E-05*
6	*3.8352E-05*	*9.2E-06*
7	*9.4899E-06*	*6.66E-07*

$$\delta = 0.048124$$

$$C_{d,i} \cong \frac{C_L^{\,2}(1+\delta)}{AR\pi} = \frac{0.79^2(1+0.048124)}{6\pi} = 0.0347$$

Then calculating the total drag coefficient gives,

$$C_d \cong 0.021 + 0.0347 = 0.0557$$

The difference between this one and the one calculated in Fluent is,

$$C_d \, difference \quad \cong \left\| \frac{0.056 - 0.062}{0.056} \right\| 100\ \% = 10.7\%$$

This is, for our purposes, an acceptable difference when considering the uncertainties involved in calculating the Drag Coefficient. This general agreement in the two methods, one using simple PLLT collocation and the other using FLUENT incompressible

turbulence code instils some confidence in a converged solution and that it is yielding valid results.

3 Computational Results

One of the earliest analysis, still relevant to this day, is the work of Hoffman and Joubert [13]. They developed a method, which parallels the turbulent boundary layer, to explain the distribution of circulation throughout the region of the tip vortex (see also Phillips [14] for similar results). Up to their time, individuals had compared their experimental results with the work of Newmans [15] laminar flow theory. Their data would be curve fit and the value of the effective viscosity would be calculated based on this curve fit. This primitive method was not very successful and now a basis of comparison has become Hoffman and Jouberts circulation model. That is,

Inner Region,

$$\frac{\Gamma}{\Gamma_c} = 1.83\left(\frac{r}{r_c}\right)^2$$

Overlap Layer,

$$\frac{\Gamma}{\Gamma_c} = 2.14\log\left(\frac{r}{r_c}\right) + 1$$

Then an Outer "defect" Region,

$$\frac{\Gamma_o - \Gamma}{\Gamma_c} = fn\left(\frac{r}{r_o}\right)$$

Where subscript 'c' indicates the core value and subscript 'o' indicates the asymptotic far value and the radius where 99% (arbitrarily) of this value is achieved. We see that the

inner two regions satisfy a universal self- similarity whereas the outer region need not (and does not).

Below, in Figure 3-1 and Figure 3-2, are shown the circulation profiles obtained in the numerical study (this circulation was calculated by integrating the vorticity over the surface), this profile is taken at $x/c = 1.2$, it is seen that both the inner region and overlap region, in the near field, both obey the universal law to high accuracy. It is observed that the inner region is at a slightly lower slope than that predicted by the universal profile, but other than that it agrees with the predicted profile satisfactorily. Also shown, in Figure 3-3, is the, azimuthally averaged, tangential velocity as computed from this circulation profile, when compared with the magnitude of the cross-flow velocity taken at given angular sections it is seen that the average profile is representative of these individual profiles. It was observed that the core radius of the tip vortex occurs at approximately $r_c/c = r/c = 0.07$.

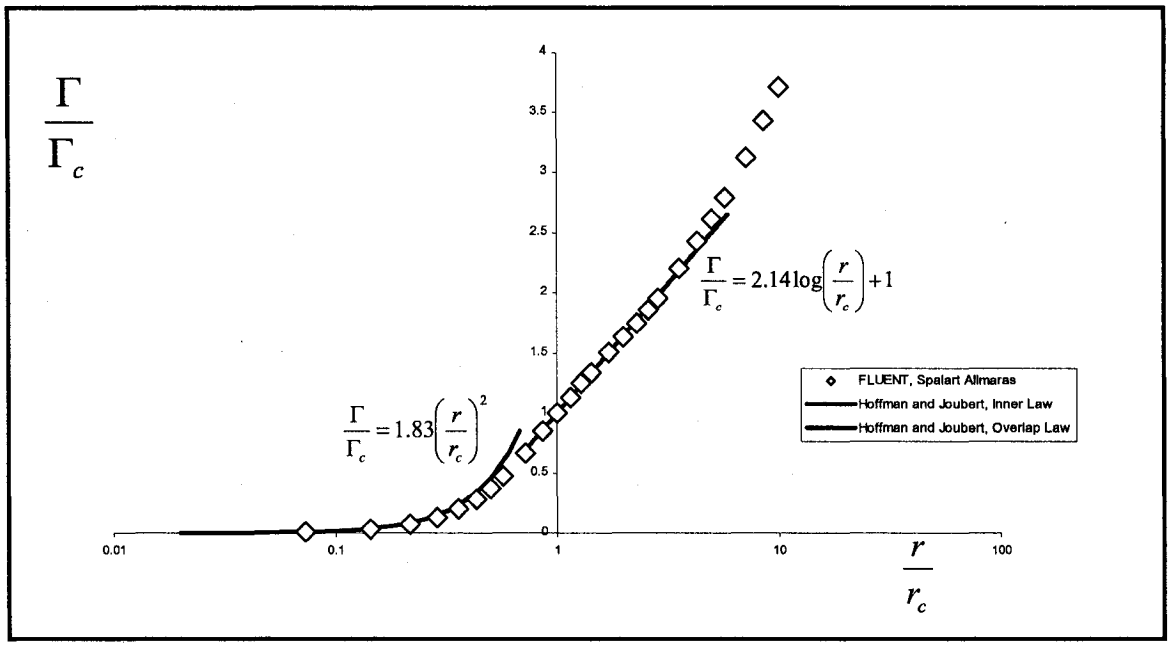

Figure 3-1: Circulation Results, X/C=1.2, Semilog Scale

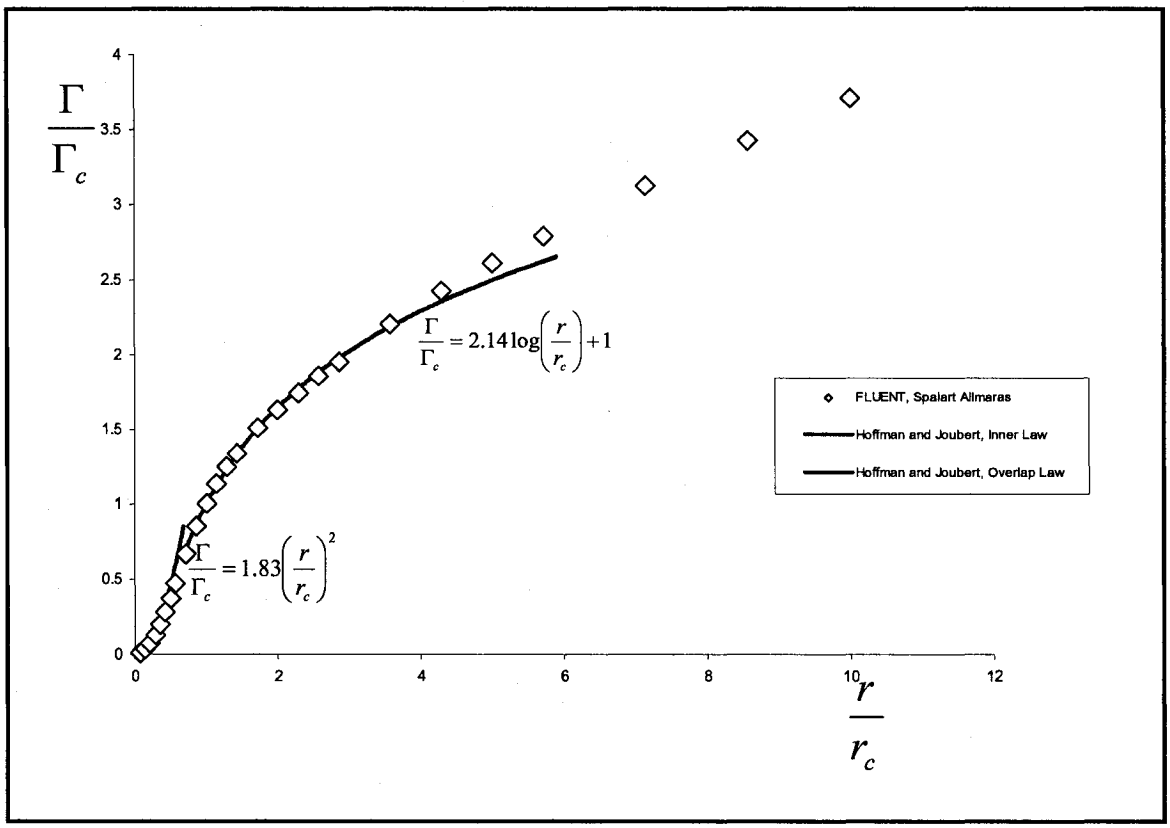

Figure 3-2: Circulation Results, X/C=1.2

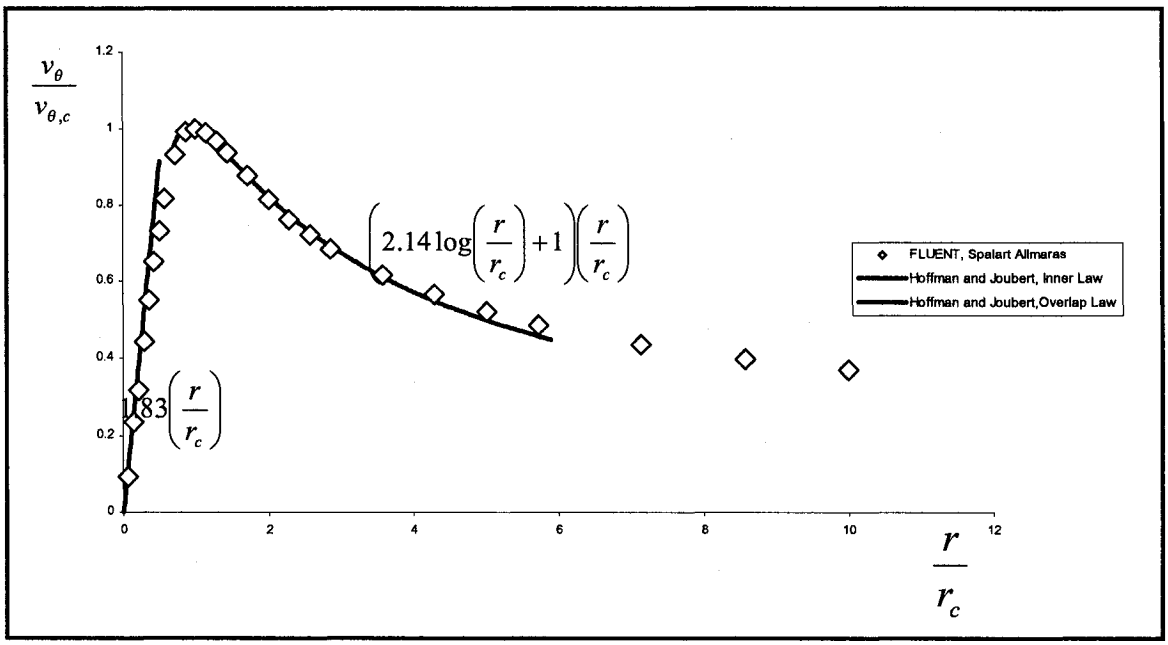

Figure 3-3: Average Tangential Velocity

Presented below, in Figure 3-4, Figure 3-5, Figure 3-6, Figure 3-7 and Figure 3-8, are contours of streamwise vorticity ξ_z, which have been non-dimensionalized, $\frac{\xi_z c}{2U_\infty}$, where c is the cord and U_∞ is the free stream velocity. Compared are those obtained from the numerical study, and those from an experiment performed by Birch [5]. The experiment was performed in a wind tunnel; also, the computational wing and the experimental are of different aspect ratio. Despite this it is apparent that the structures of the contours are similar. The contours correspond to locations along the wing, $x/c = 0.5, 0.75, 0.9, 1 \& 1.5$.

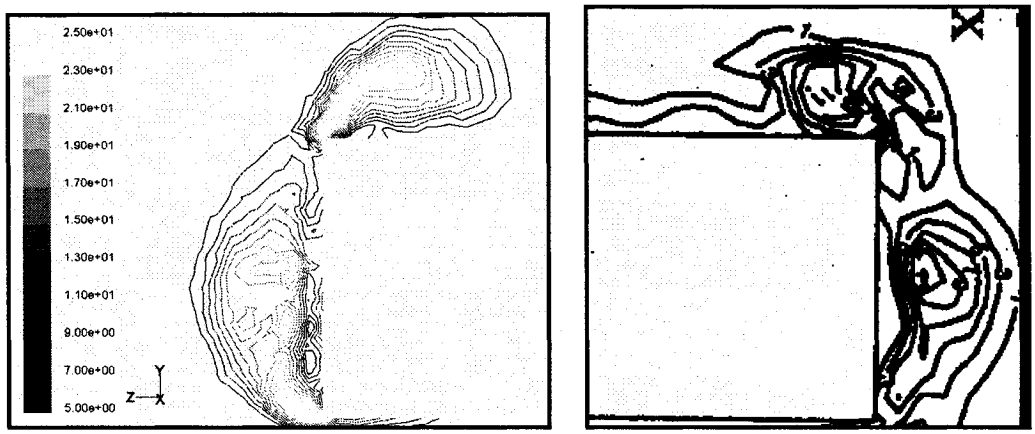

Figure 3-4: Numerical & Experimental Vorticity, $\frac{\xi_z c}{2U_\infty}$, at X/C=0.5 [5]

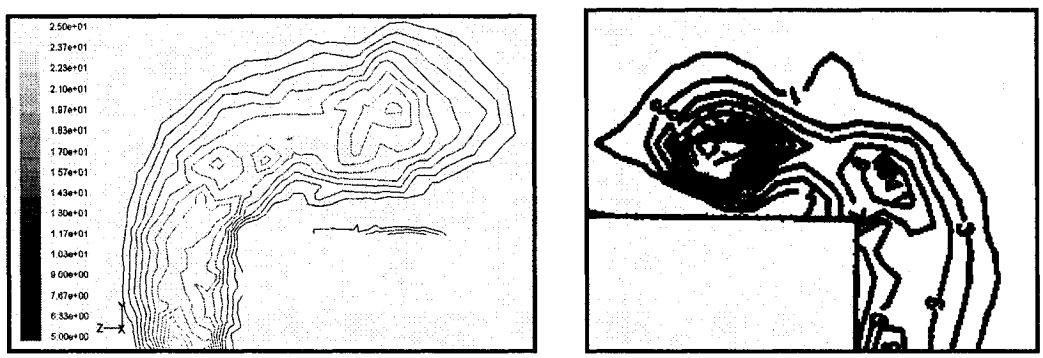

Figure 3-5: Numerical & Experimental Vorticity, $\frac{\xi_z c}{2U_\infty}$, at X/C=0.75 [5]

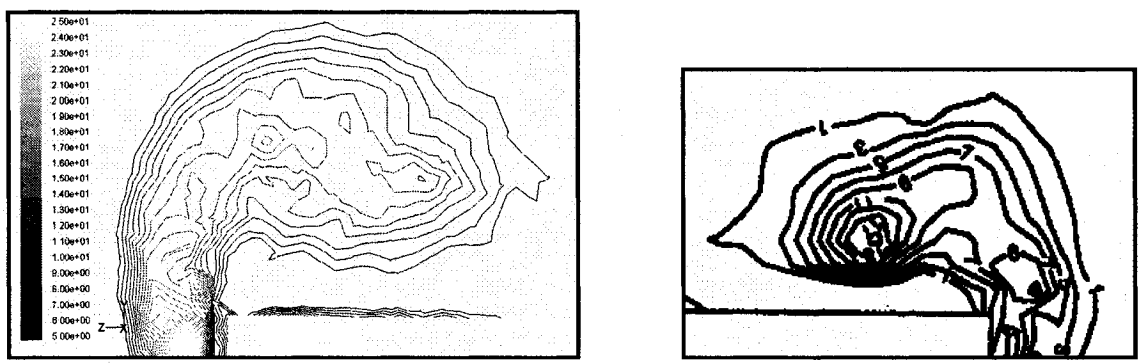

Figure 3-6: Numerical & Experimental Vorticity, $\frac{\xi_z c}{2U_\infty}$, at X/C=0.9 [5]

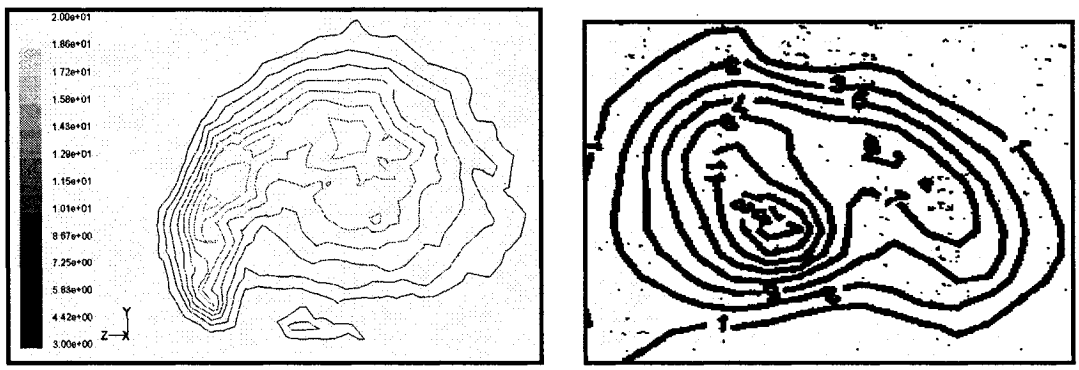

Figure 3-7: Numerical & Experimental Vorticity, $\frac{\xi_z c}{2U_\infty}$, at X/C=1 [5]

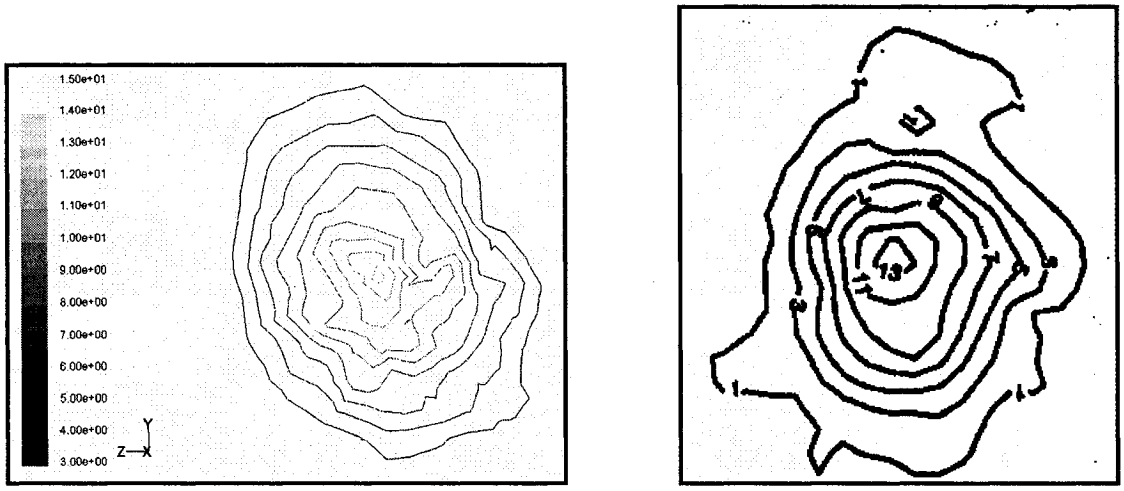

Figure 3-8: Numerical & Experimental Vorticity, $\frac{\xi_z c}{2U_\infty}$, at X/C=1.5 [5]

The worst agreement occurs at the nearest streamwise location, whereas, the furthest streamwise location is in very good agreement. Overall, it seams that the computational results have higher values of the vorticity. This can be partially attributed to the larger aspect ratio of the computational wing; higher aspect ratio wings exhibit more abrupt changes in loading at their tips, because of this, they will be more likely to shed more intense vortices from their tips than wings of lower aspect ratio. This qualitative

reasoning is consistent with the results of a wake prediction schemes, like those of Betz [16], or Rosso [17]. Also, the experimental grid on which the velocity is obtained is coarser than the computational grid on which the velocity is calculated; since numerical differencing is required to calculate the vorticity (on the computational or experimental grid), the high values achieved on the wing are then lost in the inability to resolve the high gradients. This presents another likely reason for deviations in locations of high vorticity.

Shown below, in Figure 3-9, are the filled contours of vorticity. The vortices begin to form close to the leading edge, this is attributable to the fact that this is the location along the wing that contributes most to the lifting of the surface, i.e. this location is the most aerodynamically loaded.

Francis and Kennedy [18], who investigated the Near Field, also noted similar observations to the ones obtained in this study. They used helium bubbles to visualize the process and make a very accurate detail of the roll-up. They remark the presence of swirling secondary flow first present right near the leading edge, this progresses along side the wing. Also, at approximately 60% of the chord, the vortex moves to the top of the wing and inboard. Also, see the work of Ghias et al. [10] for a recent account of this behaviour, obtained in a Large Eddy Simulation (LES).

Fluid, near the leading edge, in the vicinity of the tip, has the largest secondary pressure gradient and, in accordance, a secondary component in the flow is present. The large

pressure gradient creates an accelerating boundary layer in the cross flow direction with a very high velocity gradient, or vorticity. This can be seen, in Figure 3-11, where a large spanwise component of shear stress (which has been non-dimensionalized with the free stream dynamic pressure), $\frac{\tau_z}{1/2\rho U_\infty^{\ 2}}$, is beneath the wing, in fact it is the highest value that can be found on the wing. The boundary layer then separates from the wing surface and its high velocity gradient turns into a high vorticity vortex. Even at a distance of one tenth of the chord the vortex has accumulated, roughly, over half its circulation; This is shown in Figure 3-10. These contours were calculated by integrating circular contours of vorticity; the radius of the contours was three times the core radius found at $x/c = 1.2$ that is, $r = 3r_c\big|_{x/c=1.2}$. This corresponds to $r/c = 0.21$. As the fluid is convected downstream it accumulates more vorticity, shed from the wall. As we move downstream the strength increases but the vorticity in the core decreases, because these sections of the wing do not contain as abrupt changes in loading and because the high vorticity from the leading edge is conducive to mixing and has had a chance to diffuse.

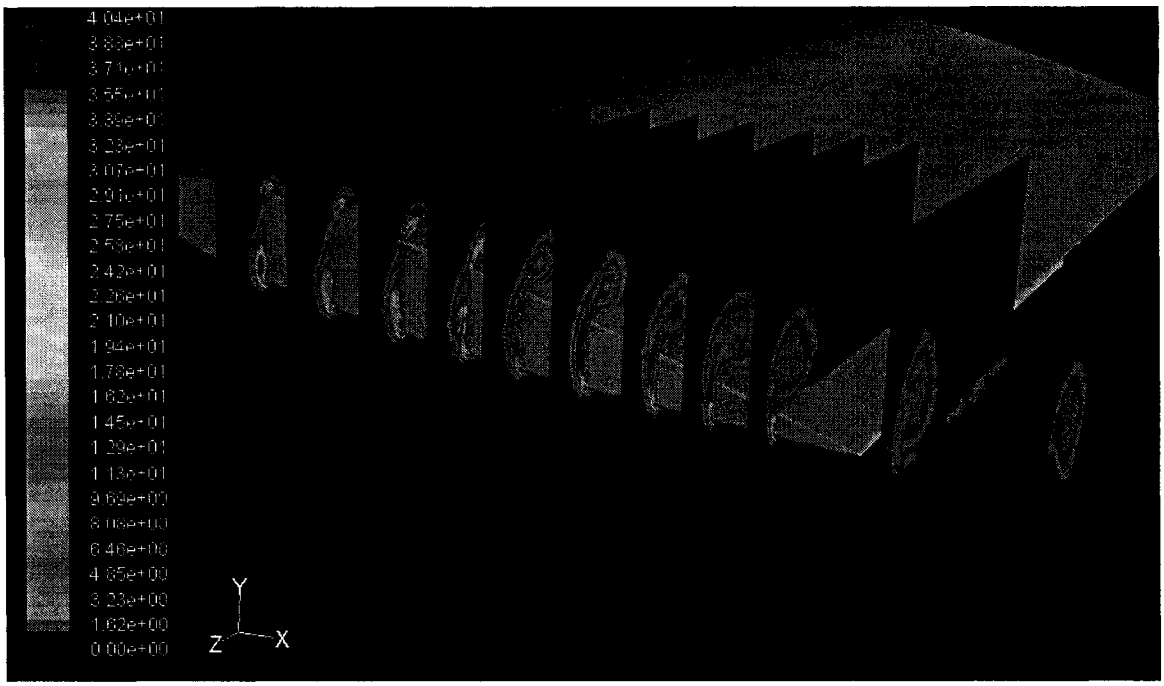

Figure 3-9: Vorticity Contours $\frac{\xi_z c}{2U_\infty}$

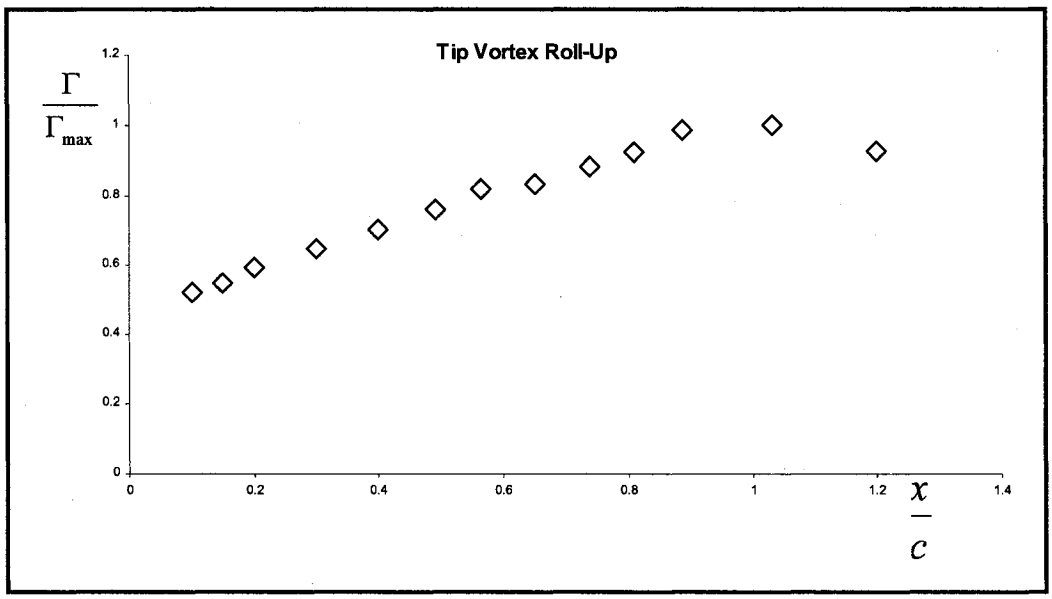

Figure 3-10: Roll-Up Process

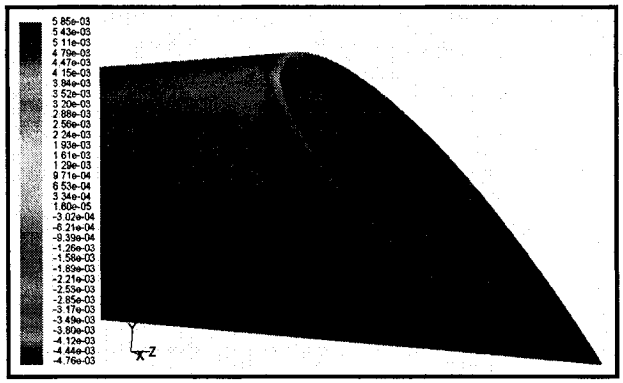

Figure 3-11: z-component Wall Shear Stress, $\frac{\tau_z}{1/2\rho U_\infty^2}$, Pressure Side

As shown in Figure 3-12, the vortex out board of the wing scrubs the side, inducing a, very light, downward shear force, as it climbs up the tip (the magnitude of this force is a very small fraction of the total lift). The local minimum, of the vertical component of skin friction (which has been non-dimensionalized with the free stream dynamic pressure), $\frac{\tau_y}{1/2\rho U_\infty^2}$, on the side of the wing, shows the approximate projected position of the vortex center, as it rises. At about 80% of the chord, the entire outboard vortex has climbed on top of the wing and has merged with the secondary vortex. Shown in Figure 3-13, the wing feels a large change in the spanwise shear stress directly under the vortex, at this chord position.

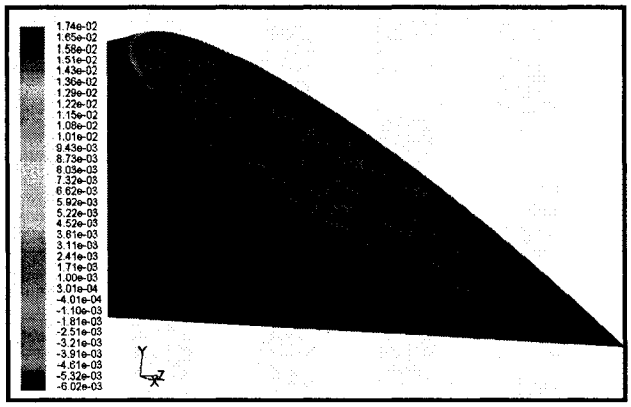

Figure 3-12: y-component, $\frac{\tau_y}{1/2\rho U_\infty{}^2}$, Wall Shear Stress

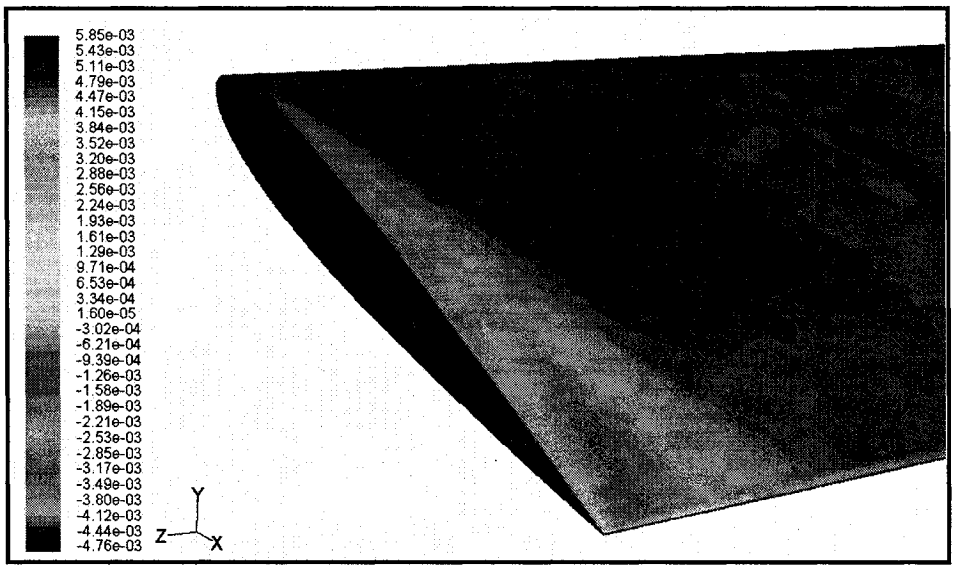

Figure 3-13: z-component Wall Shear Stress, $\frac{\tau_z}{1/2\rho U_\infty{}^2}$, Suction Side

The circulation of the inner region reaches its final value, just about, at the end of the wing. However, because there have been no abrupt changes in wing loading, the vorticity is distributing itself evenly. Even though the circulation has been continuously increasing, because the peak vorticity has been decreasing, the magnitude of the peak cross-flow velocity remains relatively constant during the entire roll-up process, at about

half the free stream value. Refer to Figure 3-14 for contour of cross-flow velocity, $\sqrt{u_y^2 + u_z^2}/U_\infty$, where u is a particular velocity component and the subscript refers to the direction of that component. The peak magnitudes compare well with experiments conducted by Birch [5] (see Figure 3-15).

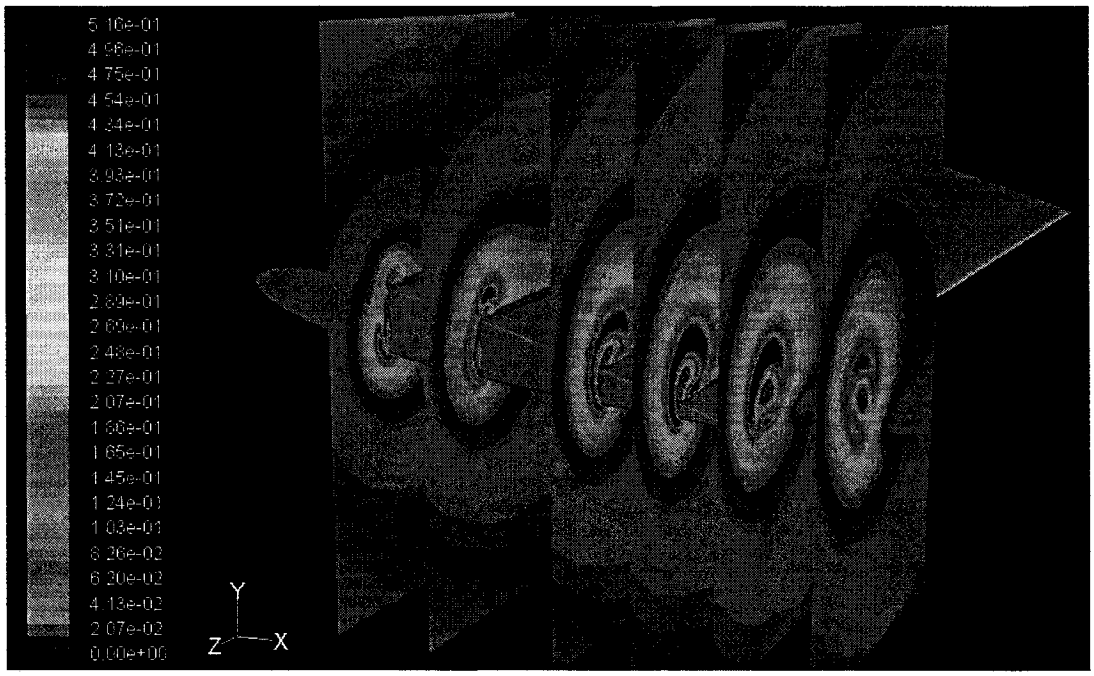

Figure 3-14: Cross Flow Velocity Contours $\sqrt{u_y^2 + u_z^2}/U_\infty$

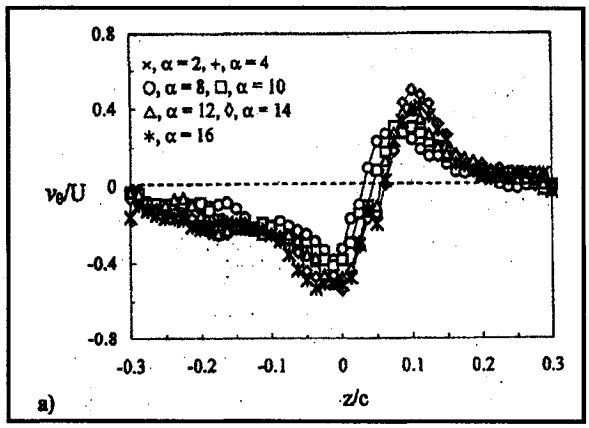

Figure 3-15: Birch, Tangential Velocity [5]

Also, it is well known that, the rotation of the fluid creates centrifugal forces that impose a radial pressure gradient. The pressure outside the fluid is fixed and serves as a boundary condition; this results in the fluid inside the vortex having a pressure that is below the externally imposed pressure.

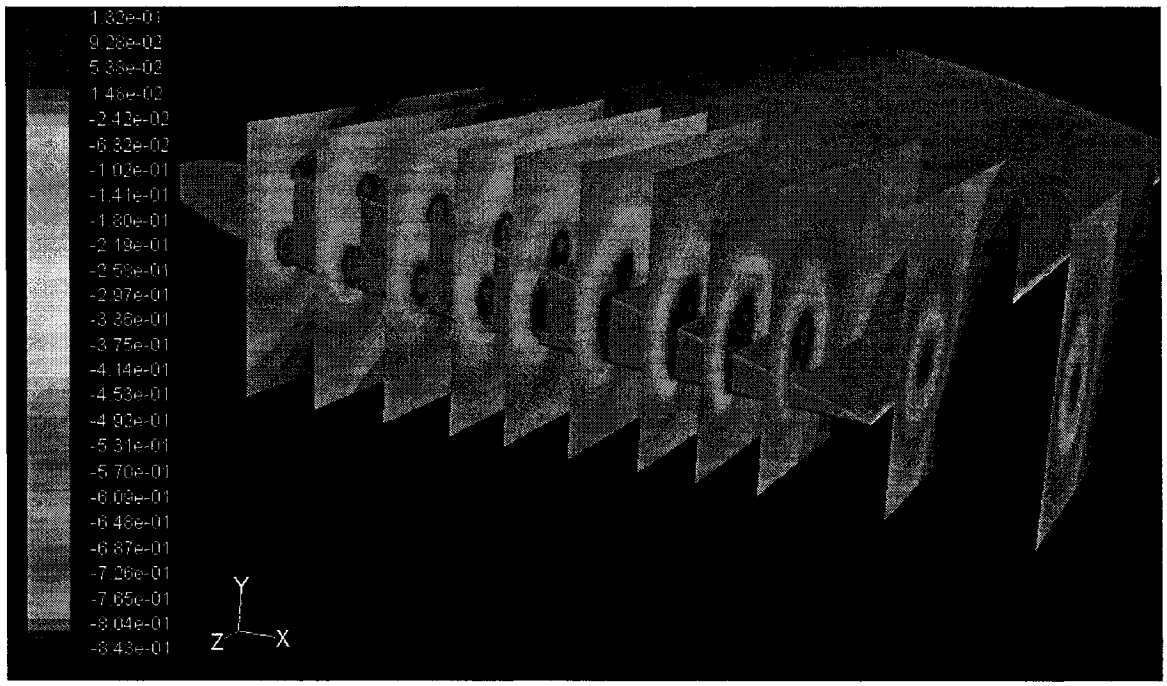

Figure 3-16: Static Pressure Contours $\frac{p-p_\infty}{1/2\rho U_\infty{}^2}$

The low pressures displayed in the non-dimensional static pressure contours, $\frac{p-p_\infty}{1/2\rho U_\infty{}^2}$, (see Figure 3-16) where p is the static pressure and p_∞ is the free stream static pressure, clearly depict the presence of the two vortices; by the time the vortex leaves the trailing edge the vortices have merged into one and the pressure contours are very nearly axisymmetric, even though the velocity contours are less so. It can be shown, by

inspection of the Navier-Stokes equations, that small velocity perturbations will be balanced by even smaller pressure perturbations.

Because much of the fluid in the tip vortex has been in the wing boundary layer, where dynamic pressure is low, it is defective in terms of total pressure. When the vortex has left the wing, the (total pressure) losses in the core will be, on the order of, over half its dynamic pressure, as can be seen in Figure 3-17.

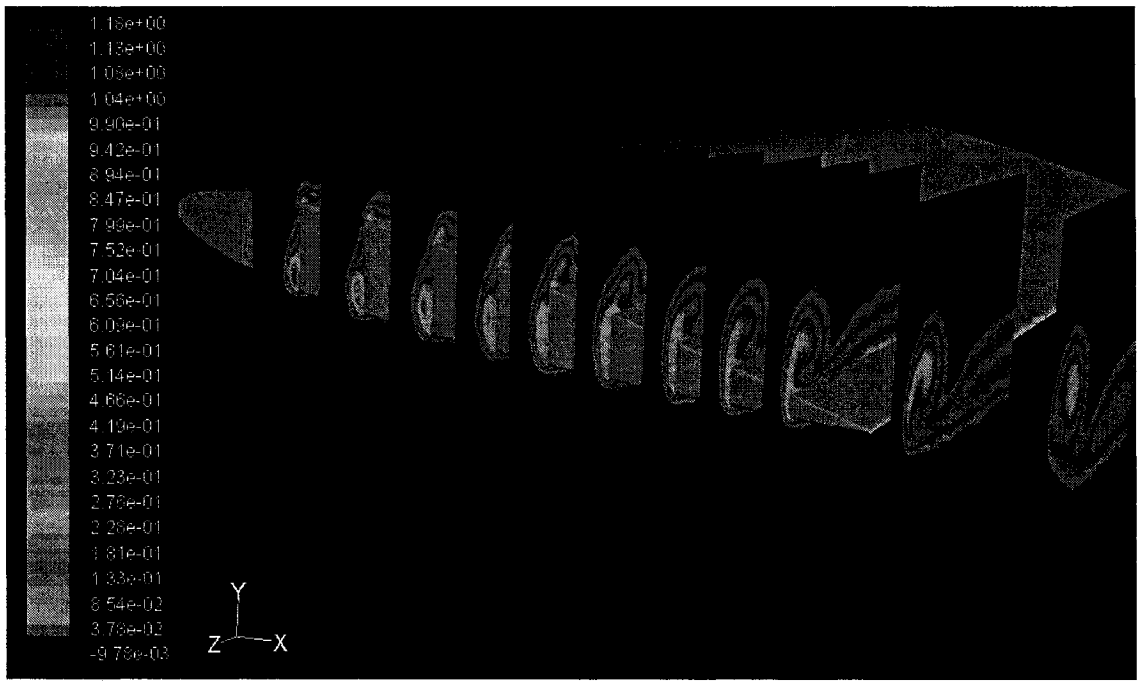

Figure 3-17: Total Pressure Loss, $\left(\frac{p_\infty - p}{1/2\rho U_\infty^{\,2}}\right)+\left(1-\frac{u_x^{\,2}+u_y^{\,2}+u_z^{\,2}}{U_\infty^{\,2}}\right)$, Contours

Since the tangential profile is dictated by a nearly universal profile of all trailing vortices and the static pressure is dictated by this, the difference between the tangential velocities contribution to the total pressure and the actual total pressure (which is dictated by total pressure losses of the boundary layer) contributes to the axial velocity excess (or defect).

As a result, the axial velocity has been known to exhibit either surplus or deficit with respect to the free stream value, depending on the amount of losses.

Bachelors' theory [19] is a statement of this; the pressure, dynamically, links the tangential velocity and axial velocity; the celebrated equation takes on the simple form,

$$u_x^{\,2} = U_\infty^{\,2} + \int_r^\infty \frac{1}{(2\pi r)^2} \frac{\partial(\Gamma^2)}{\partial r} dr - 2\Delta H$$

Where ΔH is the total pressure losses divided by the fluid density and all other terms have been previously defined. The terms on the right represent, the contribution to the axial velocity from the free stream, the contribution to the axial velocity from the swirling motion, and the decrease in the axial velocity due to the presence of losses, respectively.

The axial velocity contours, u_x/U_∞, of Figure 3-18, as well as the loss contours show us that the tip vortex is rolling up the wake as it leaves the trailing edge of the wing. This behavior is responsible for the erratic overshooting and undershooting in axial velocity data in the near field seen in experiments (see Figure 3-19); every time an entire oscillation is seen, it may be assumed that a layer of wake has been crossed. It is also interesting to note that even though the tip vortex is rolling up wake, when taking the vorticity contours into consideration, it is shown that the addition in strength of the vortex is small and only contributes to its outer layers.

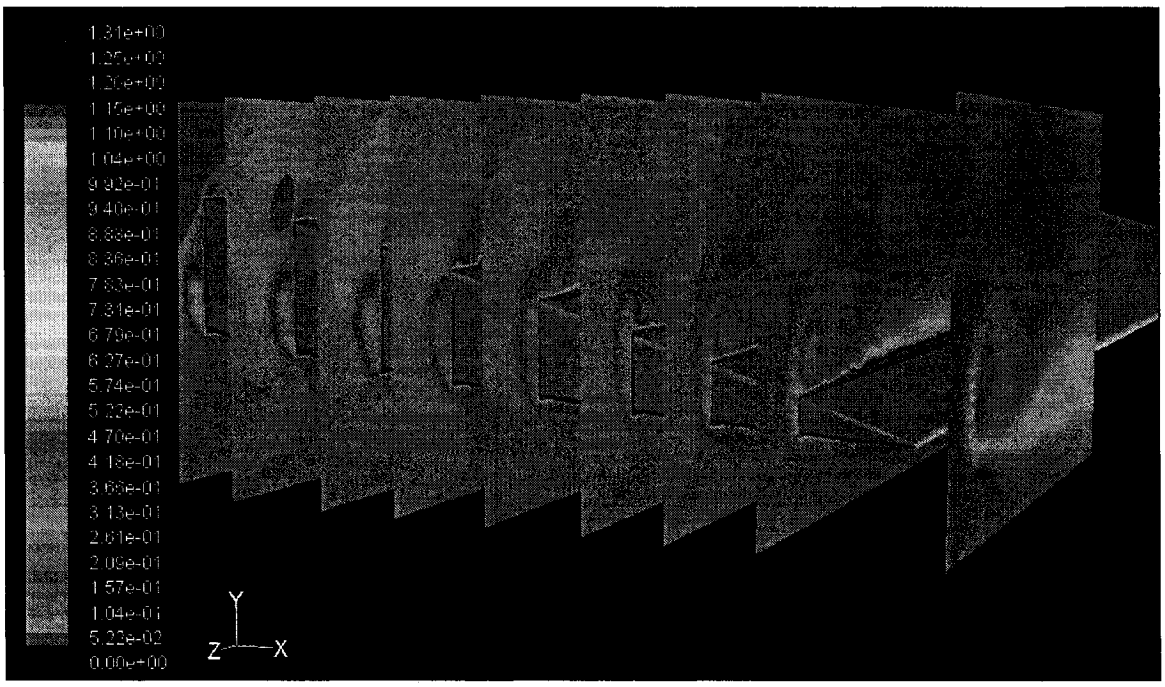

Figure 3-18: Axial Velocity Contours, u_x/U_∞

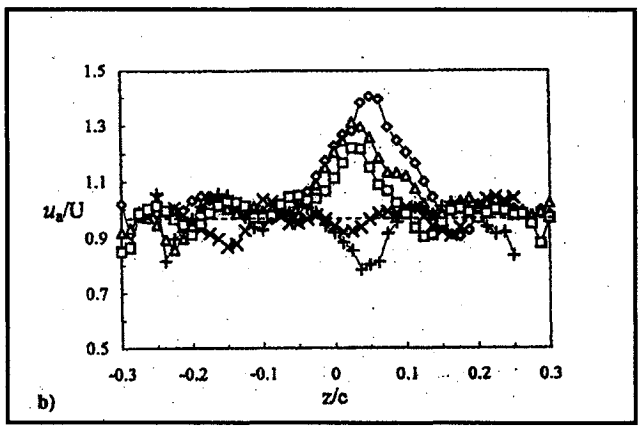

Figure 3-19: Birch, Axial Velocity [5]

Below are presented two isosurfaces of vorticity, Figure 3-20 and Figure 3-21; the first one is a high vorticity isosurface, the structure depicted are the two separate vortices. The second isosurface is of much lower vorticity and it depicts the Roll-Up of the, so-called,

vortex sheet. Again, this depicts that the final tip vortex will gain the majority of its strength from the structures created by the leading edge, and while still on the wing.

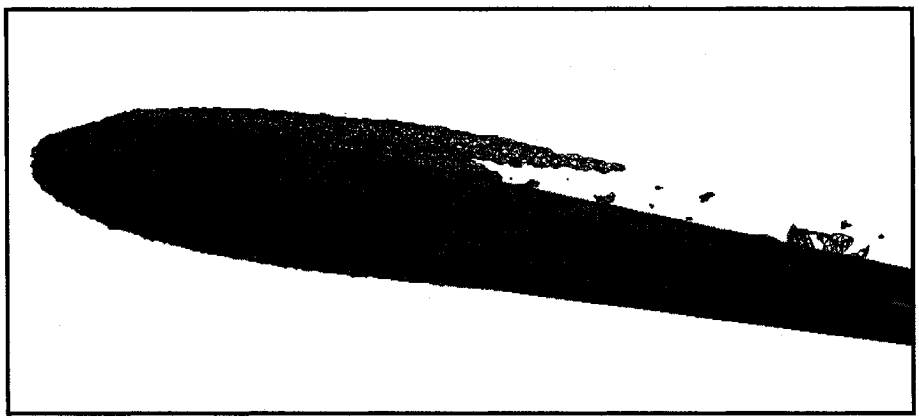

Figure 3-20: High Vorticity Isosurface

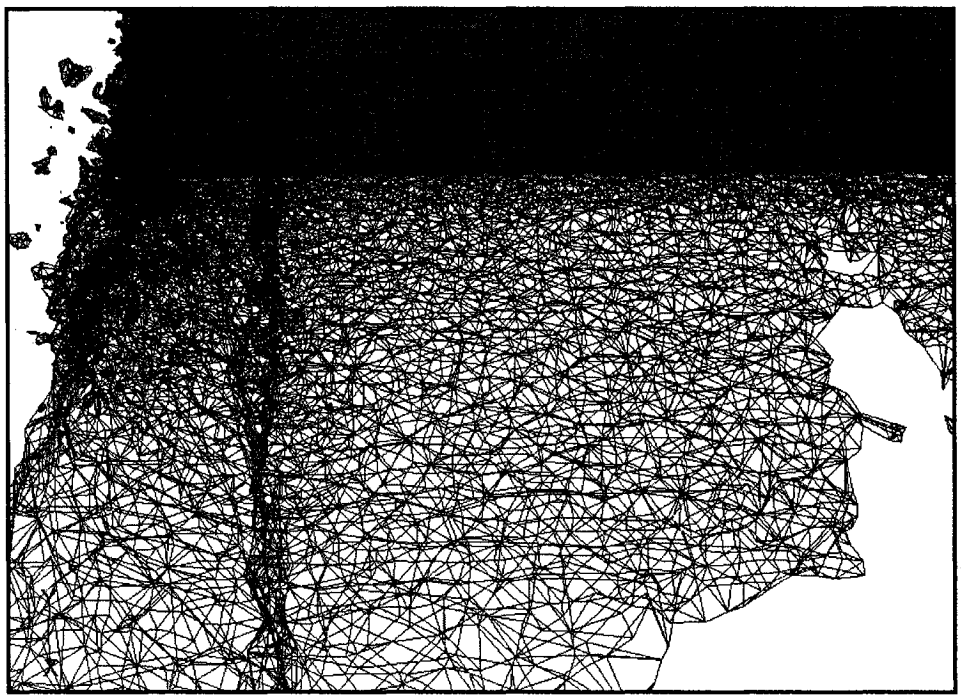

Figure 3-21: Low Vorticity Isosurface

4 Analysis

In 1972, Moore and Saffman [20], [21] produced a theory describing the variation of vortex characteristics with wing loading and downstream position. This theory and its results are summarized in what follows. Their work was restricted to laminar flows with low wing loading,

$$v_\theta << U_\infty$$

where v_θ is the tangential component of velocity and U_∞ is to represent the free stream velocity, found away from the wing. By dynamical necessity, resulting from this restriction, the axial velocity perturbation will also be small,

$$u = U_\infty + \Delta u \cong U_\infty$$

where, u represents the axial velocity and Δu is the perturbation of axial velocity from the free stream value. This allows them to turn the three dimensional problem into an unsteady two dimensional problem where,

$$t = U_\infty / z$$

where z is the axial position to which a given particle has convected in time t. Local tip loading is assumed to take on the form,

$$\Gamma_w = 2(\Gamma_r \gamma) x^{1-n}$$

Where n is a dimensionless constant, Γ_w is the circulation at a given section, x, inboard from the wing tip. Γ_r is the circulation of the root section, that we should observe will scale linearly with angle of attack, if it is low enough, and γ has the same units as x^{1-n}. Based on this, a sheet of strength, κ, where,

$$\kappa = \frac{d\Gamma}{dx}$$

is shed from the wing. All of this is quite palatable and more or less in line with potential flow theory. By dimensional considerations, they then assume that the circulation in the tip vortex is of the form,

$$\Gamma = 2(\Gamma_r \gamma)(\lambda r)^{1-n}$$

r is the radial distance from the center to a given point in the vortex and λ is a dimensionless scaling factor. The tangential velocity follows as,

$$v_\theta = \Gamma/(2\pi r) = \frac{(\Gamma_r \gamma)(\lambda)^{1-n}}{\pi} r^{-n} = \beta r^{-n} \text{ , say,}$$

Since vortex lines move with the fluid, their displacement will be,

$$\frac{r\Delta\theta}{t} = \beta r^{-n}$$

$$r = \left(\frac{t\beta}{\Delta\theta}\right)^{1/n+1}$$

$\Delta\theta$ is the tangential displacement of a given fluid particle at radial position r and time t. Considering this is the case, it is then reasonable that the vortex length scale as,

$$r_c \propto (\beta t)^{1/n+1}$$

if there is an approximate balance between radial pressure gradient, $\frac{\partial p}{\partial r}$, and centrifugal force. This results in,

$$\frac{\partial p}{\partial r} = \rho(\beta r^{-n})^2 / r$$

$$p = \frac{-\rho\beta^2 r^{-(2n)}}{2n}$$

When this is integrated from zero to infinity; these approximations are in line with a boundary layer problem, in that, the pressure in the viscous core is being imposed from the inviscid portion. The next step can be effectively summarized in arguing that these

conditions are imposed far away from the core ($r \to \infty$) and linearized boundary layer type equations in cylindrical coordinates are solved.

From this, the tangential velocity decays as,

$$v_\theta = 0.49\beta\left(\frac{x}{c}\right)^{-0.25}(RE)^{-0.25}$$

and the core grows as,

$$r_c = 2.92\left(\frac{x}{c}\right)^{0.5}(RE)^{0.5}$$

c is the wing cord and $RE = U_\infty c/\nu$ is the Reynolds number flow parameter with ν being the kinematic viscosity. The significance of these results to the present study are that the tangential velocity scales linearly with angle of attack and that the core radius is altogether independent of the angle of attack.

The conditions used in the derivation dictate the region of applicability of these expressions. It was the restrictions of small perturbation that allowed for the transformation of the three dimensional problem into a two dimensional one and that allowed for the applicability of the linearized equations of motion to apply. It has been shown very clearly by Batchelor (summarized later) that variation in axial velocity is necessary when there are large tangential velocities. Under these conditions the transformation of Moore and Saffman break down. Therefore, the regions of applicability are restricted to locations of low tangential velocity. This implies, that the expressions apply far enough from the wing (large streamwise distance and large Reynolds number) that the velocity has decayed to an acceptable level and that this critical distance, at

which it will begin to apply, decreases with decreasing wing loading and, therefore, with decreasing lift and, furthermore with the angle of attack.

4.1 Dimensional Analysis

It is desirable to obtain the dependence of the vortex with angle of attack, as the tangential velocity becomes increasingly higher. For this purpose, it will be hypothetically increased to the point that it is many orders of magnitude larger than the streamwise component,

$$v_\theta >> U_\infty$$

This will be done to the point that the upstream streamwise component, U_∞, is negligibly small and its only functional importance is that it implicitly aids in the generation of lift.

Now that the problem has been set up, we may list all variables and parameters of primary importance and we construct the most general form of our functional relationship. For the time being we have placed only one characteristic parameter describing the geometry of the tip, and have designated it to be *TG*. It may be assumed that its dimensions are that of either length or area. Also, for the sake of simplicity, the main source of shear stress is due to the, molecular, kinematic viscosity, and for this reason the only flow parameter will be the Reynolds number; this will be generalized in a subsequent section.

$$v_\theta = fn(r, r_c; L, \rho, \nu, cb, TG)$$

Where L is the lift, ρ is the density, b is the span, r_c is the location of maximum tangential velocity, called the core radius and all other variables have been previously defined. For this purpose, four dimensionless groups are sufficient, (when considering that the core radius is a variable which is to be expressed as a function of all other variables). We shall restrict ourselves to cases that scale as follows,

$$\frac{\rho v_\theta{}^2 cb}{L} = fn(RE_\theta, TG^*, \frac{r}{r_c})$$

where $RE_\theta = v_\theta r_c / v$ For this case and $TG^* = TG/cb$, as we can see, the streamwise velocity does not scale with the tangential velocity; this is justified because the magnitude of the tangential velocity is so great that a variation in streamwise velocity will not be felt (when maintaining the lift constant). Then, by dimensional necessity, it must scale with lift. It is immediately apparent that the pressure gradient (as produced by lift) is the driver of the tangential component of velocity and if it were not present the tangential velocity would identically be zero. When we consider, by analogy, the flow around a sharp bend in a channel, the streamlines are quite similar to the streamlines of the tip vortex projected in the cross-flow plane (see Figure 4-1). In fact the dimensional analysis yields similar parameters. The flow in the loss affected (defective in terms of total pressure) region, which is going to make up much of the core region, is attempting to negotiate the bend. Since the bend is sharp, a local region of large pressure gradient is created (or in the case of a flat tip two local regions of large pressure gradient), which causes separation of the secondary flow (or two local separations). This separation is what initiates the tip vortex (or two coherent vortices, initially, on the flat tip).

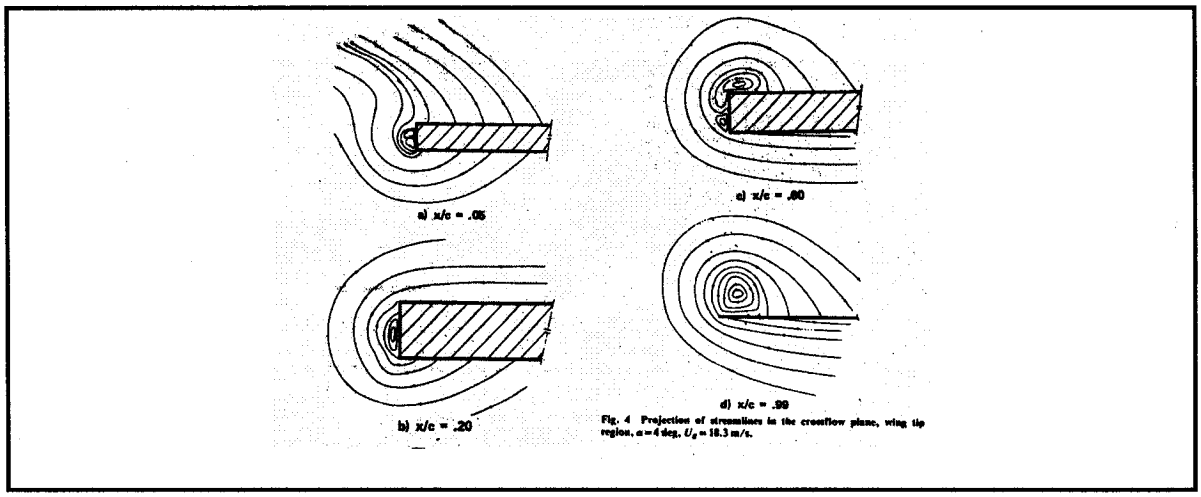

Figure 4-1: Stream Lines, Projected into the Cross Flow Plane [18]

Since it is well established that in a conduit,

$$\Delta p \propto \rho U^2$$

Δp being the pressure drop across the bend and U being the mean velocity. By analogy, for the case of a tip vortex in the near field, taking a projection in the cross-flow plane yields,

$$\Delta \bar{p} \propto \rho v_\theta{}^2$$

Where the characteristic pressure difference, $\Delta \bar{p}$, is,

$$\Delta \bar{p} = \left(\bar{l}'\right)\frac{1}{c} = \left(\frac{L}{b}\right)\frac{1}{c}$$

where we see $\bar{l}'$ is the average sectional lift. This analogy for the pressure difference is valid if the sectional lift coefficient is relatively constant up until the vicinity of the tip, such that $\bar{l}' \cong l'$, where the "vicinity of the tip" is of the same order of magnitude as the size of the vortex. As a result, large tip loading is required to make this analogy valid. For this, hypothetical case, this is consistent with the requirement that the tangential velocity

be extremely high, since it is required that the circulation on the wing change very abruptly to cause this intense vortex.

Observed in the non-dimensionalization is the requirement that the characteristic dimension of the tip scales with the planform area. Also, any subsequent tip dimensions that would be included in the analysis would also need to scale with this, or possibly, with a previously defined tip characteristic.

Also we notice that there is no dependence on the aspect ratio. Since the loading is heavy, the sectional lift coefficient towards the center of the wing is approximately constant; in this case, the effect (on the tip vortex) of further increasing the span is negligible. This is justifiable because towards the centerline there is negligible change in span loading, and then, no vorticity is shed from this section. For this reason, in this particular regime, the functional relation between the tip vortex and the aspect ratio is negligible.

This may be expressed more conveniently as,

$$\frac{1}{C_L}\left(\frac{v_\theta}{U_\infty}\right)^2 = fn(RE_\theta, TG^*, \frac{r}{r_c})$$

In this case we see,

$$\left(\frac{v_\theta}{U_\infty}\right) = (C_L)^{0.5}\, fn(RE_\theta, TG^*, \frac{r}{r_c})$$

Restricting ourselves to the case where we are operating at a low enough angle of attack we would see that,

$$C_L = a_o(\alpha - \alpha_o)$$

And our expression takes on the relatively simple form,

$$\boxed{\frac{v_\theta}{U_\infty} = (\alpha - \alpha_o)^{0.5} f_1(TG^*) f_2(RE_\theta) G\left(\frac{r}{r_c}\right)} \quad (1)$$

Immediately, an assumption has been made that a separation of variables solution is possible. This is because we are constraining ourselves to a specific regime of the flow, namely, this scaling is asymptotically approached as the tip vortex strength becomes high. For this reason, we expect this scaling to be approached at higher angles of attack and lower Reynolds number and streamwise position.

Similarity in the radial direction has been modeled to scale with the core radius, the location of maximum velocity; this is a good similarity variable, which has been observed to be successful in tip vortex flow experiments as well as other types of vortex flows. This is because an isolated vortex has no external geometry to scale with and would have no preferential ability to change profile. In the near field, unfortunately, this self-similarity is not as strong as what is observed far away from the point of tip vortex genesis. This lack of perfect coherence results from the presence of another characteristic geometry, namely, the wing. For this reason, values of core radius and peak tangential velocity sited in the above expressions actually correspond to the circumferentially averaged values when compared to the experimentally observed quantities.

We see that square root variation serves as an asymptotic state; if there was flow only in the cross flow plane (with the same pressure gradient being applied) it would be satisfied exactly (as has been observed in other pressure driven flows), however, the increased presence of the streamwise component, as a result of the process of decay or the

reduction of lift, act to reduce the ratio of v_θ / U_∞, in a manner which causes the value of the exponent to increase until it reaches another asymptote, of linear scaling, as obtained in the work of Moore and Saffman. Their results are summarized in the form,

$$\boxed{\frac{v_\theta}{U_\infty} = (\alpha - \alpha_o) f_3\left(RE_c, \frac{x}{c}\right) G\left(\frac{r}{r_c}\right)} \quad (2)$$

It is assumed that the profile shape has not significantly changed from the near to far field regime, this could be revisited in future studies. Shown in Figure 4-2, Figure 4-3, Figure 4-4 and Figure 4-5 are various profiles, which are shown to all scale with different exponents, all varying between 1 and 0.5.

Also, when looking at the profiles, we make the observation that the data becomes more scattered as the approximate value of exponent decreases, this is consistent with the notion that as the exponent decreases we are approaching the point of vortex initiation.

It should be explicitly stated that, perhaps, neither of these scaling laws are satisfied in any given experiment, however, the claim is that as the tip vortex strength is increased a square root variation is approached, whereas, at lower vortex strength a linear variation is approached. Because the first regime, of square root scaling, requires higher tangential velocities, it is approached when we are closer to the wing, before the decay process has taken effect and, also, as the lift, and thus, angle of attack is increased (but still when it is below its stalling condition). Whereas, the second regime, of linear scaling is approached far away or at low angle of attack.

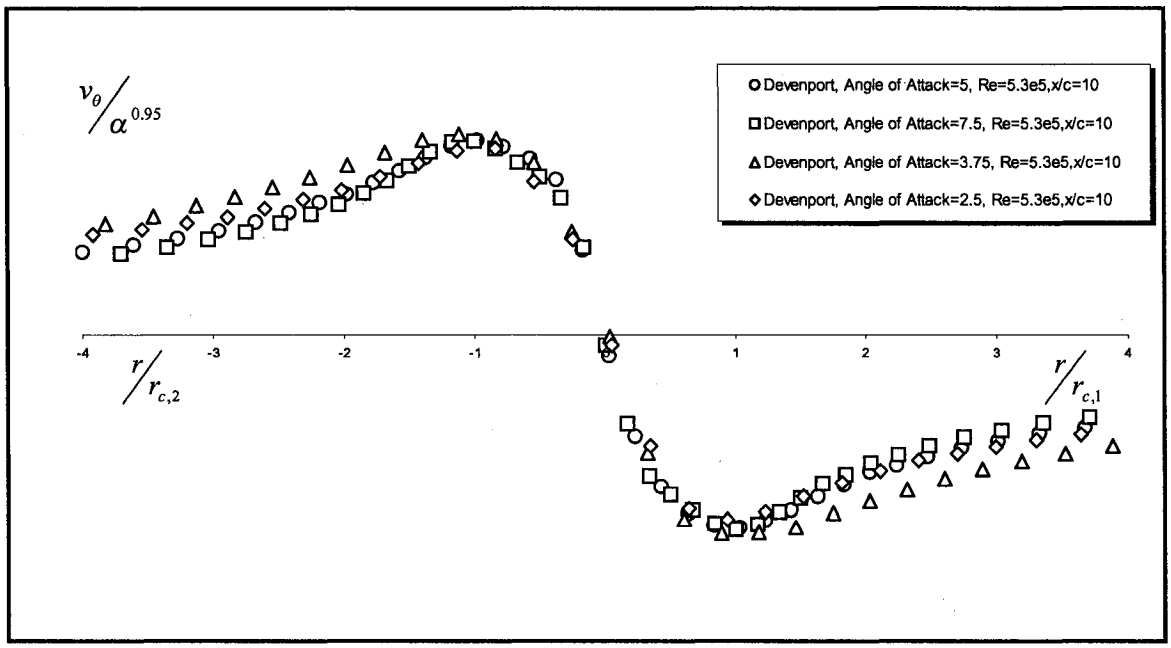

Figure 4-2: Devenport, Tangential Velocity [26]

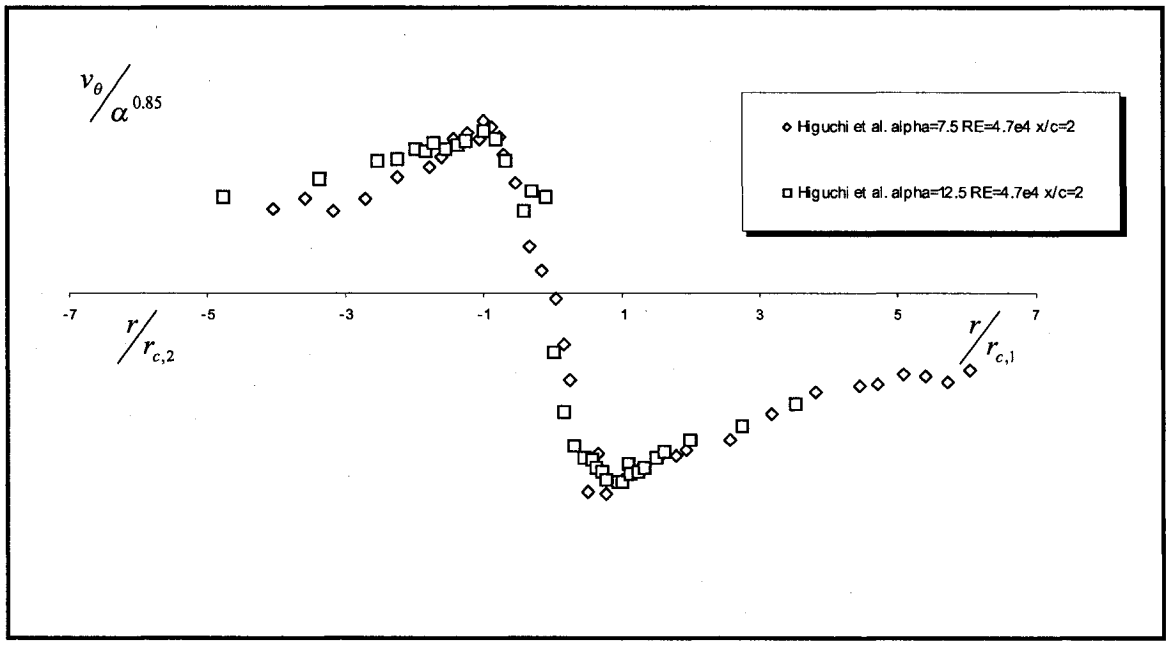

Figure 4-3: Higuchi et al., Tangential Velocity [27]

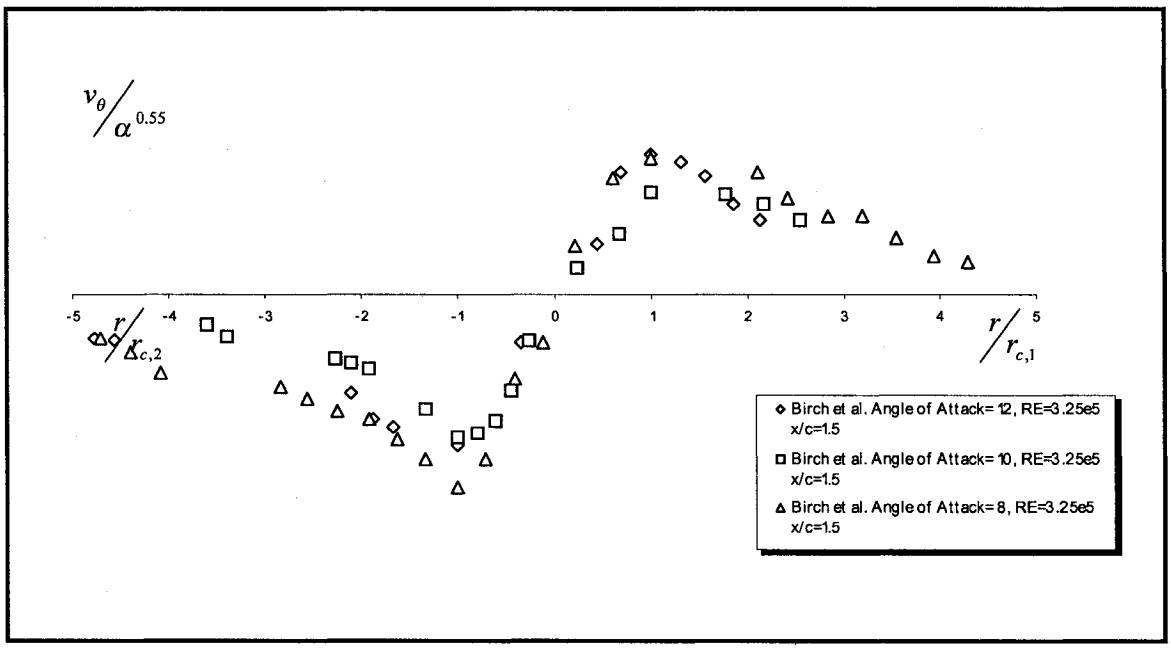

Figure 4-4: Birch, Tangential Velocity [4]

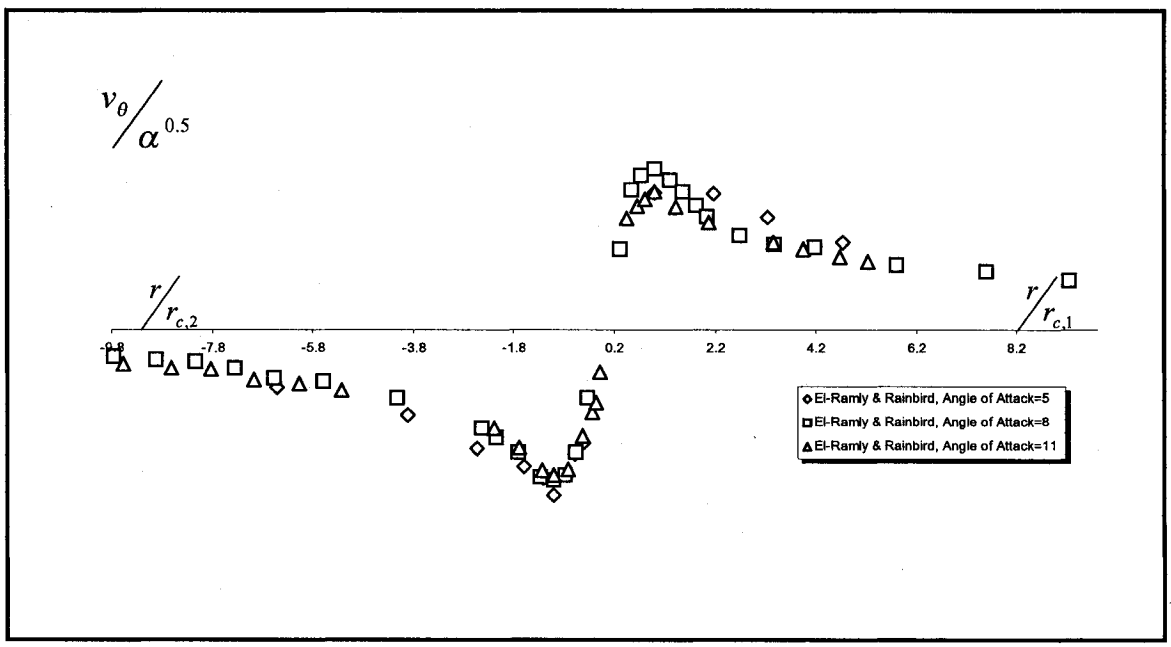

Figure 4-5: El-Ramly & Rainbird, Tangential Velocity [28]

4.2 Intermediate Regime

Now that the lower and upper asymptotes have been obtained, it remains to match these two conditions, such that, the region where these two regimes are in balance may be obtained. In what follows, a general mathematical analysis is carried out; any physical interpretation to the variables is postponed until the results are obtained.

In general, if scaling is as,

$$\frac{v_\theta}{U_\infty} = {\alpha_E}^m F_{12} G$$

in, what we choose to call, the asymptotic Near Field regime, whereas if,

$$\frac{v_\theta}{U_\infty} = {\alpha_E}/{F_3}\, G$$

expresses the asymptotic Far Field regime, assuming that the variable, G, does not change in either case. A deviation from the Far Field regime would probably be very well expressed by,

$$\frac{v_\theta}{U_\infty} = f\left({\alpha_E}/{F_3}\right) G$$

$$\frac{v_\theta}{U_\infty} = f(\eta) G$$

Where, $\eta = {\alpha_E}/{F_3}$

And a deviation from the Near Field regime would probably be very well expressed by,

$$\alpha_E{}^m F_{12} G - \frac{v_\theta}{U_\infty} = g\left(\alpha_E{}^m F_{12}\right) G$$

$$\frac{v_\theta}{U_\infty} = (\xi - g(\xi)) G$$

Where, $\xi = \alpha_E{}^m F_{12}$

For conditions which are balance with these two regimes, we should expect,

$$f(\eta) = \xi - g(\xi)$$

Taking the derivative with respect to, α_E and then multiplying by α_E,

$$\frac{\partial f(\eta)}{\partial \eta}\frac{\partial \eta}{\partial \alpha_E}\alpha_E = \frac{\partial \xi}{\partial \alpha_E}\alpha_E - \frac{\partial g(\xi)}{\partial \xi}\frac{\partial \xi}{\partial \alpha_E}\alpha_E$$

$$\frac{\partial f(\eta)}{\partial \eta}\eta = m\left(\xi - \frac{\partial g(\xi)}{\partial \xi}\xi\right)$$

We observe that the left hand side is, at most, solely a function, η, and the right hand side is, at most, solely a function of, ξ. Since this is the case both sides are actually equal to a constant. For this reason we obtain,

$$\frac{\partial f(\eta)}{\partial \eta}\eta = K$$

$$m\left(\xi - \frac{\partial g(\xi)}{\partial \xi}\xi\right) = K$$

These two equations may be integrated to obtain,

$$f(\eta) = K\ln(\eta) + B$$

$$g(\xi) = \xi - \frac{K}{m}\ln(\xi) + A$$

this yields two separate, but equivalent, expressions for the tangential velocity,

$$\boxed{\frac{v_\theta}{U_\infty} = \left(\frac{K}{m}\ln(\xi) - A\right)G = (K\ln(\eta) + B)G} \quad (3)$$

Now, we take our above states, equations (1) & (2), as approximately satisfying the asymptotic conditions required for the intermediate region to be modeled by the equations presented in (3).

Upon comparing with the expressions in (1) & (2) it is shown,

$$m = 0.5, \alpha_E = \alpha - \alpha_o, F_{12} = f_1(TG^*) f_2(RE_\theta), F_3 = {}^{1}\!/\!_{f_3\left(RE_c, {}^{x}\!/\!_{c}\right)}, G = G\left({}^{r}\!/\!_{r_c}\right)$$

A, B and K are all "pure" constants, for this restricted case. However, expressing the velocity in terms of the Far Field variables, $\eta = {}^{\alpha_E}\!/\!_{F_3}$, is more convenient because, at a given stream Reynolds number, it is clear that the Far Field variable varies linearly with angle of attack (Recall $F_{12} = f_1(TG^*) f_2(RE_\theta)$ is a function of $v_\theta \ldots$ etc, which vary with angle of attack).

Let us assume that the dimensional analysis that has been performed does not sufficiently satisfy the conditions for a given experiment. Perhaps other flow parameters are needed to sufficiently describe the test conditions, namely, a turbulence parameter. Let it be observed, that there are but two minimum requirements for the above model to apply, they are,

1) That the Near Field and the Far Field have different scaling, with angle of attack, this was demonstrated in the figures above to be a fundamental quality.

2) That the Near Field and Far Field scale with different variables (or functions), what has been called F_{12} and F_3. This can be easily satisfied by the fact that in the Near Field the tip vortex is a function of the specific tip geometry. Whereas, far away from the wing the tip vortex should only feel the effective "lifting line", which is solely a function of the wing planform shape and not the tip shape.

4.3 Core Tangential Velocity

The Far Field and Intermediate Field regimes may be generalized as taking on the form,

$$\boxed{\frac{v_\theta}{U_\infty}\frac{1}{G} = \alpha^* = fn\left(\frac{\alpha_E}{F_3}\right)} \quad (4a)$$

where,

$$\alpha^* = \frac{\alpha_E}{F_3} \text{ in the Far Field}$$

$$\alpha^* = K\ln\left(\frac{\alpha_E}{F_3}\right) + B \text{ in the Intermediate Regime}$$

Evaluating (4) at its maximum results in $v_\theta = v_{\theta,\max}$, $G\left(r/r_c\right) = G(1)$,

$$\boxed{\frac{v_{\theta,\max}}{U_\infty}\frac{1}{G(1)} = \alpha^*} \quad (4b)$$

$G(1)$ will be given its physical interpretation in a subsequent section. Data is presented in Figure 4-6 and Figure 4-7, displaying the value of (4b) in all three regimes. The constants K and B can be assessed from such a sample. It is a relatively easy matter to assess the value of K, which is found to be $K \cong 0.5$. The value of B is much more difficult to approximate (and probably much less "universal"), but is approximated at $B \cong 0.77$.

Also observed is how the very Near field data is seen to fit into the defect region. As the angle of attack is decreased or the streamwise distance and Reynolds number increased the points slide down the curve until the asymptotic, low wing loading, solution of Moore and Saffman is reached.

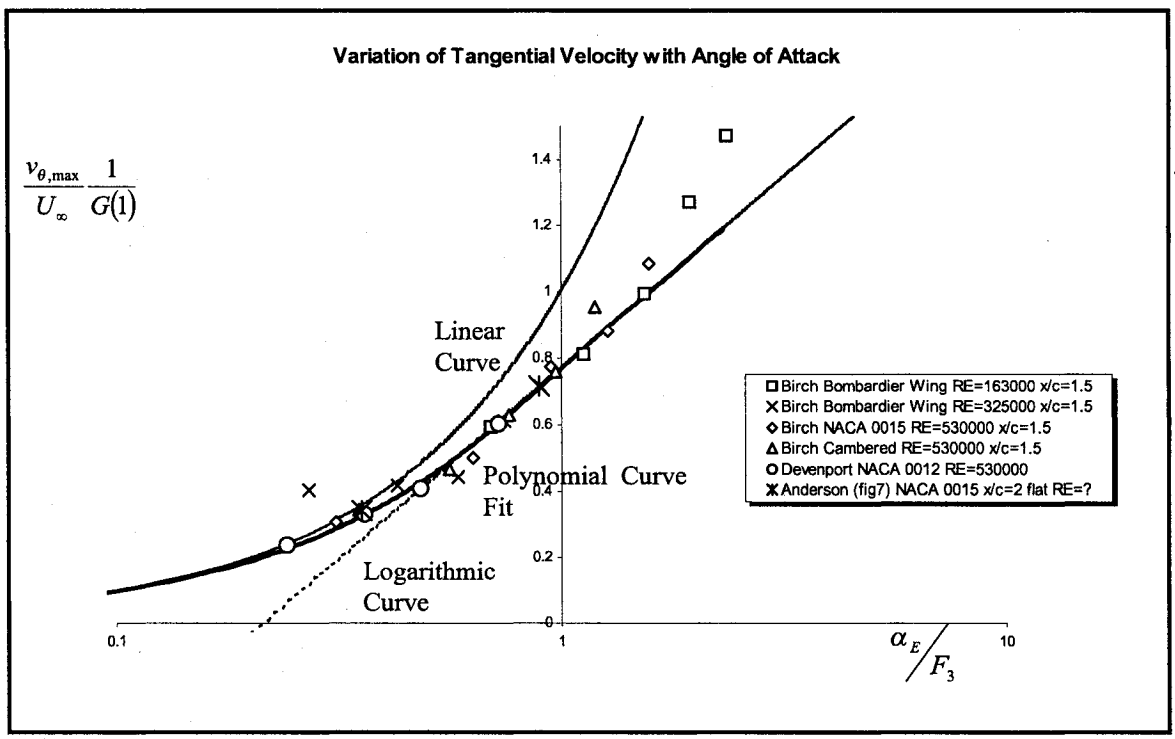

Figure 4-6: Variation of Tangential Velocity with Angle of Attack, Semilog Scale

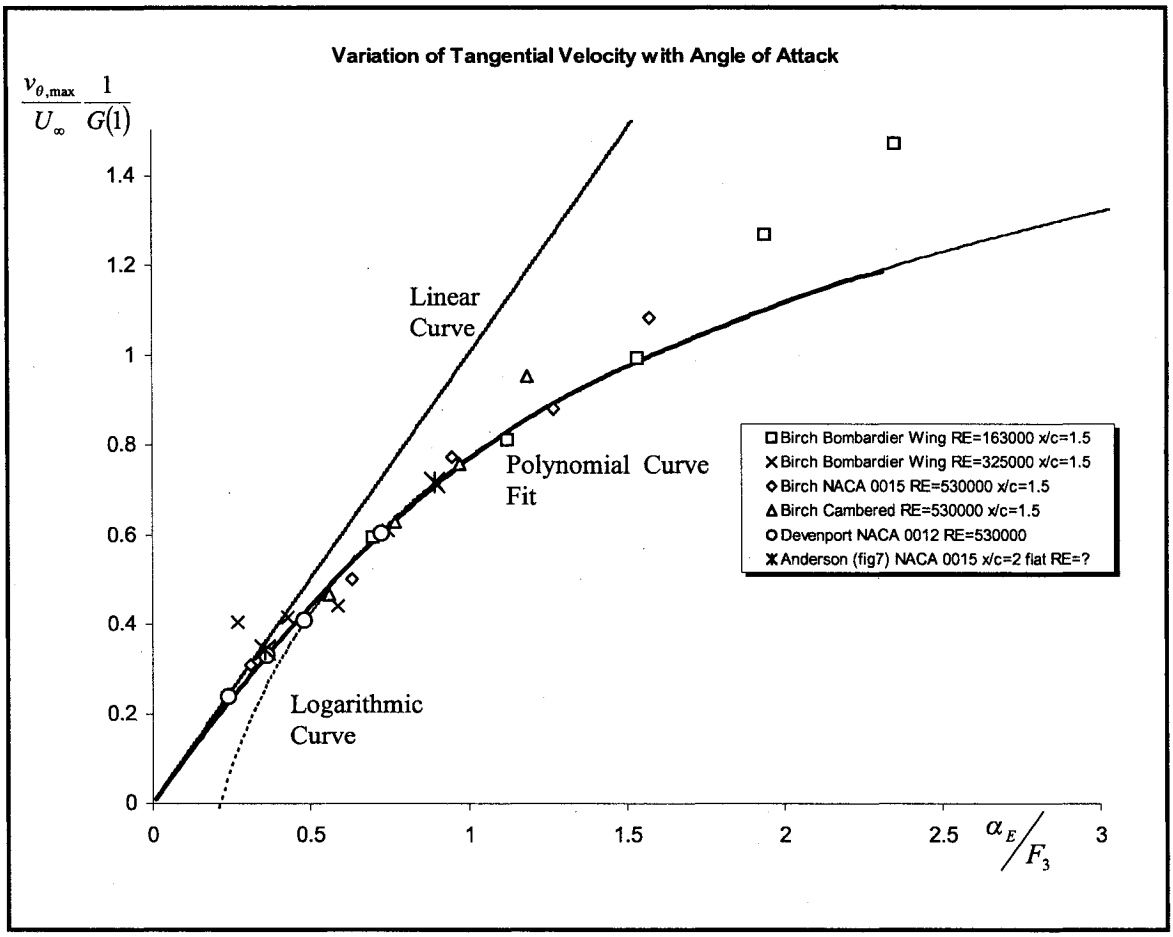

Figure 4-7: Variation of Tangential Velocity with Angle of Attack

4.4 Curve Fitting

The curve fit on the data could be a transcendental function of the form,

$$\frac{\alpha_E}{F_3} = \frac{v_\theta}{U_\infty}\frac{1}{G} + \exp\left(-\frac{B}{K}c\right)\left(\exp\left(\frac{v_\theta}{U_\infty}\frac{1}{GK}\right) - 1 - \frac{v_\theta}{U_\infty}\frac{1}{GK} - \frac{\left(\frac{v_\theta}{U_\infty}\frac{1}{GK}\right)^2}{2}\right)$$

for small values of tangential velocity an expansion about $\frac{v_\theta}{U_\infty}\frac{1}{G} = 0$ yields,

$$\frac{\alpha_E}{F_3} = \frac{v_\theta}{U_\infty}\frac{1}{G} + O^3$$

which is in total agreement with the far field expression.

Now that we have established the ability of this function to approximate the Far Field behavior of the tip vortex it is required to show that it may also be used to approximate the intermediate regime. To do this, the approach taken will be to choose the value of, c, such that the square error between the curve that has been proposed and the logarithmic model is minimized in the region of applicability. It is observed, experimentally, that the logarithmic region occurs between $\frac{v_\theta}{U_\infty}\frac{1}{G} = B$ and $\frac{v_\theta}{U_\infty}\frac{1}{G} = 2B$, therefore, this will be the domain over which the error will be minimized.

To do this we need the total error, therefore, we integrate (add up) the local error over the domain of interest, denoting $u = \frac{v_\theta}{U_\infty}\frac{1}{G}$

$$e = \int_B^{2B} \left(\exp\left(\frac{u-B}{K}\right) - u + \exp\left(-\frac{B}{K}c\right)\left(\exp\left(\frac{u}{K}\right) - 1 - \frac{u}{K} - \frac{\left(\frac{u}{K}\right)^2}{2} \right) \right)^2 du$$

We wish to find the value of the parameter, c, which minimizes this error. In order to achieve this we find the root of the first derivative of the error function with respect to c. The first derivative is,

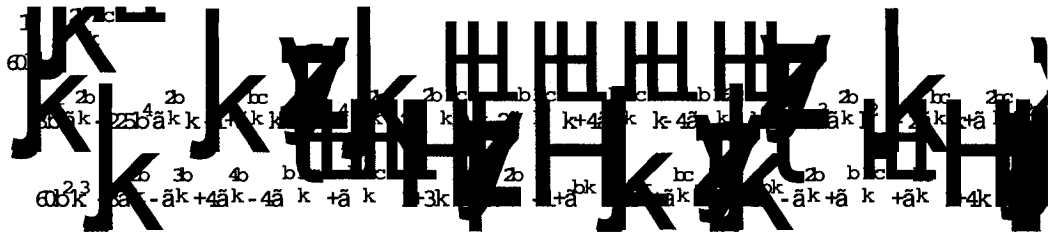

next we set it equal to zero and solve for the value of c that allows us to obtain this minimum. Doing this yields, c equal to,

(note that in this expression Log denotes the natural logarithm, in this thesis Log, usually, denotes the base 10 logarithm and Ln is reserved for the natural logarithm)

$$k\,\mathrm{Log}\left[\frac{2\left(280b^3+\frac{93b^5}{k^2}+\frac{225b^4}{k}+180b^2k+60b^2e^{b/k}k-240b^2e^{\frac{2b}{k}}k+60bk^2+120e^{b/k}k^3-150e^{\frac{2b}{k}}k^3+30e^{\frac{4b}{k}}k^3\right)}{5\left(45b^4+12b^2k+56b^3k-48b^2e^{b/k}k+36b^2k^2+24k^3-36e^{b/k}k^3+24be^{b/k}k^3-48be^{\frac{2b}{k}}k^3+12e^{\frac{3b}{k}}k^3-24e^{b/k}k^4+24e^{\frac{2b}{k}}k^4\right)}\right]$$

b

with the values of B and K as previously determined, this yields the value of $c = 0.91766$. This value could satisfactorily be used in the curve fitting of the data in the figure above. This curve is displayed in Figure 4-8 below; also shown below, in Figure 4-9, is the value of the square error between $\frac{v_\theta}{U_\infty}\frac{1}{G} = B$ and $\frac{v_\theta}{U_\infty}\frac{1}{G} = 2B$, again, it is more than satisfactory for its desired use.

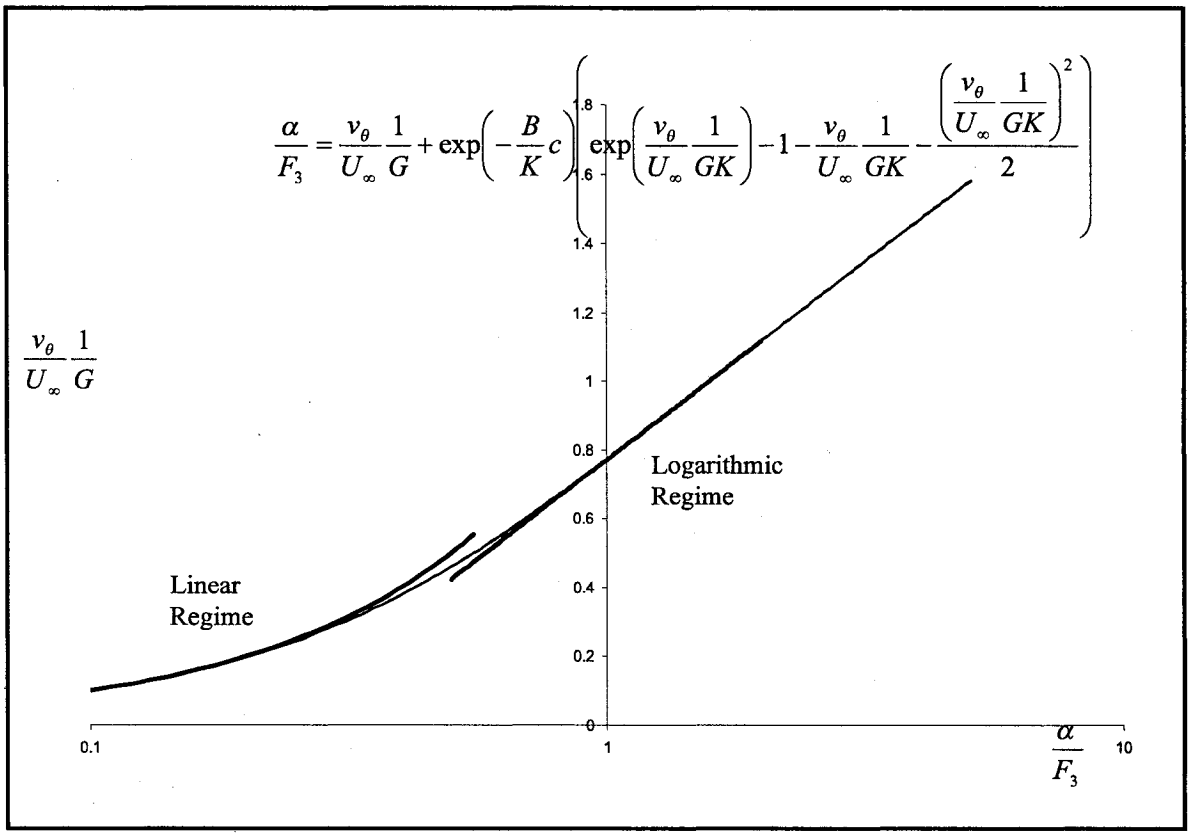

Figure 4-8: Variation of Tangential Velocity with Angle of Attack, Implicit Function

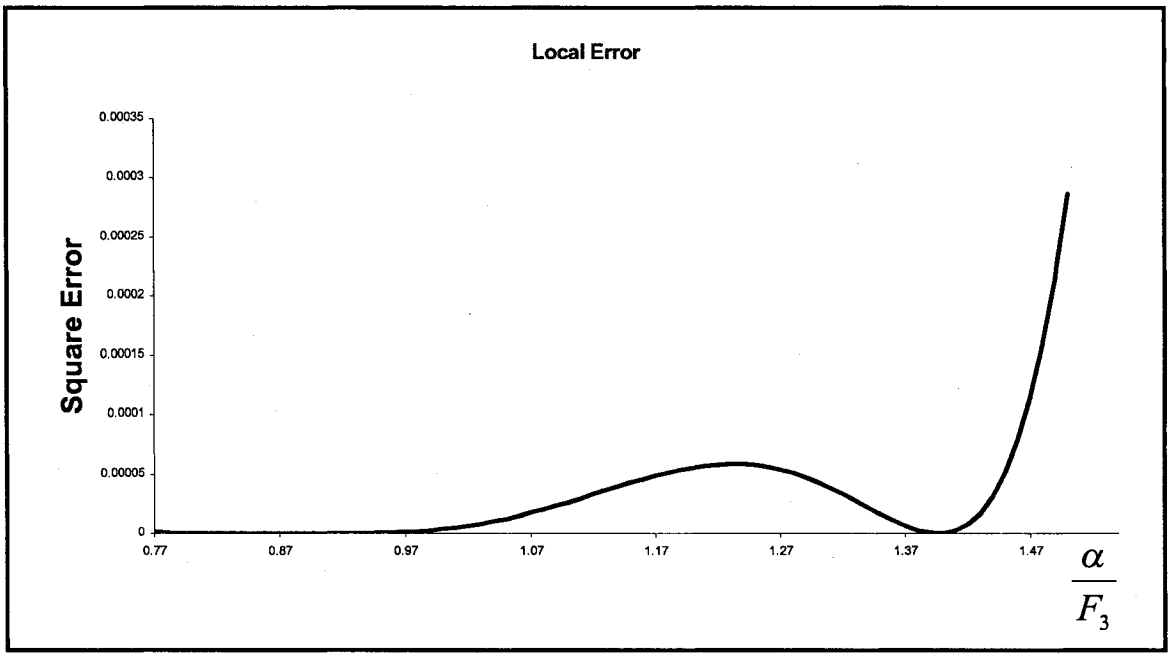

Figure 4-9: Local Error, Implicit Function

One unattractive aspect of the proposed curve is that it takes on an implicit form. Because of this, it does not lend itself to algebraic manipulation. To alleviate this problem we will propose a polynomial curve fit of the form,

$$\boxed{\frac{v_\theta}{U_\infty}\frac{1}{G} = \frac{\alpha_E}{F_3} + \sum_{i=2}^{6} a_i \left(\frac{\alpha_E}{F_3}\right)^i}$$

which, contains five undetermined coefficients. It is desired that our proposed curve be linear in the far field and logarithmic in the intermediate regime. It is observed, experimentally that this linear regime ends at about B/2 and from this point the logarithmic regime begins shortly. The logarithmic or Intermediate regime then extends until the Near Field regime begins, which has a square root dependence with angle of

attack but is multiplied by the Near field variables. In this particular curve fit we reduce the error with respect to the logarithmic curve up until $\frac{\alpha_E}{F_3} = 3B$. In this case our error is,

$$e = \int_0^{B/2} \left(\frac{\alpha_E}{F_3} - \left(\frac{\alpha_E}{F_3} + \sum_{i=2}^{6} a_i \left(\frac{\alpha_E}{F_3} \right)^i \right) \right)^2 d\left(\frac{\alpha_E}{F_3} \right) + \int_{B/2}^{3B} \left(\left(K \ln\left(\frac{\alpha_E}{F_3} \right) + B \right) - \left(\frac{\alpha_E}{F_3} + \sum_{i=2}^{6} a_i \left(\frac{\alpha_E}{F_3} \right)^i \right) \right)^2 d\left(\frac{\alpha_E}{F_3} \right)$$

we then minimize this function and solve for the parameters a_i, that allow for the minimization. These parameters are going to be expressed as a function in terms of K and B. To do this we construct the system,

$$\frac{\partial e}{\partial a_i} = 0 \text{ for } i=2..6$$

and solve it. This gives the following functional relationship for the parameters,

(note that in this expression Log denotes the natural logarithm, in this thesis Log, usually, denotes the base 10 logarithm and Ln is reserved for the natural logarithm)

```
a2 :=
        1
  15676416 B^2
   (5 (8583435 B - 56726960 K - 1472240 K Log[2] + 31352832 K Log[3] + 5588352 K Log[4] - 8890560 K Log[16] + 7112448 K Log[64] +
       14535920 K Log[B]));
a3 :=
       1
  - 35271936 B^3
   (5 (36774885 B - 241280240 K - 7846608 K Log[2] + 125411328 K Log[3] + 29338848 K Log[4] - 45722880 K Log[16] +
       35562240 K Log[64] + 44098320 K Log[B]));
a4 :=
        1
  23514624 B^4
   (55 (1436995 B - 10303360 K - 392112 K Log[2] + 5225472 K Log[3] + 1448832 K Log[4] - 2222640 K Log[16] + 1693440 K Log[64] +
       1449840 K Log[B]));
a5 :=
        1
  - 246903552 B^5
   (11 (21362775 B - 166889360 K - 7126000 K Log[2] + 83607552 K Log[3] + 26078976 K Log[4] - 39513600 K Log[16] +
       29635200 K Log[64] + 18818800 K Log[B]));
a6 :=
        1
  17777055744 B^6
   (715 (2495535 B - 21007120 K - 979440 K Log[2] + 10450944 K Log[3] + 3556224 K Log[4] - 5334336 K Log[16] + 3951360 K Log[64] +
       1947120 K Log[B]));
```

When we plug in $K = 0.5$ and $B = 0.77$ we obtain the numerical values of the parameters (see Table 7). The advantage of having the symbolic form of the parameters is that the polynomial expression should be able to support minor modifications to the universal constants, once further experimental data is made available.

Table 7: Polynomial Curve Fit Parameters

Parameter	Value
a_2	*-0.3245*
a_3	*0.315528*
a_4	*-0.3709*
a_5	*0.176842*
a_6	*-0.02865*

Presented in Figure 4-10, Figure 4-11, are plots of the curve and plots of local errors. Recall, the local error is the curve compared with the desired curve, this kept in mind, we compare the curve with a the linear regime from $0 < \frac{v_\theta}{U_\infty}\frac{1}{G} < B/2$ and with the logarithmic curve from $B/2 < \frac{v_\theta}{U_\infty}\frac{1}{G} < 3B$

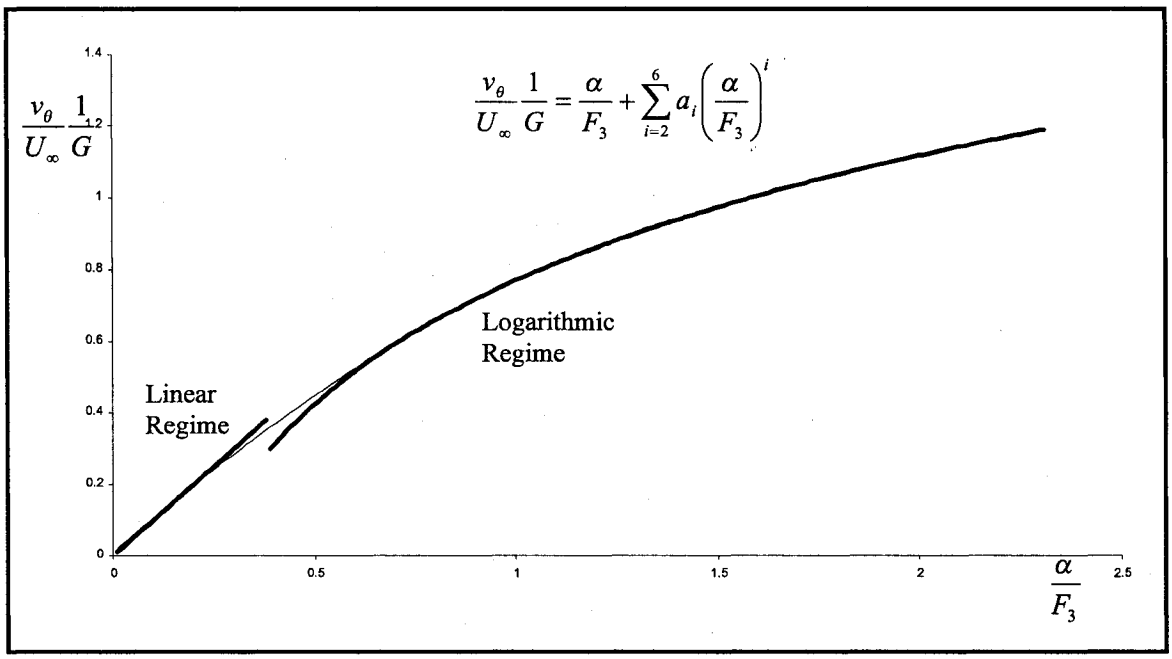

Figure 4-10: Variation of Tangential Velocity with Angle of Attack, Polynomial Function

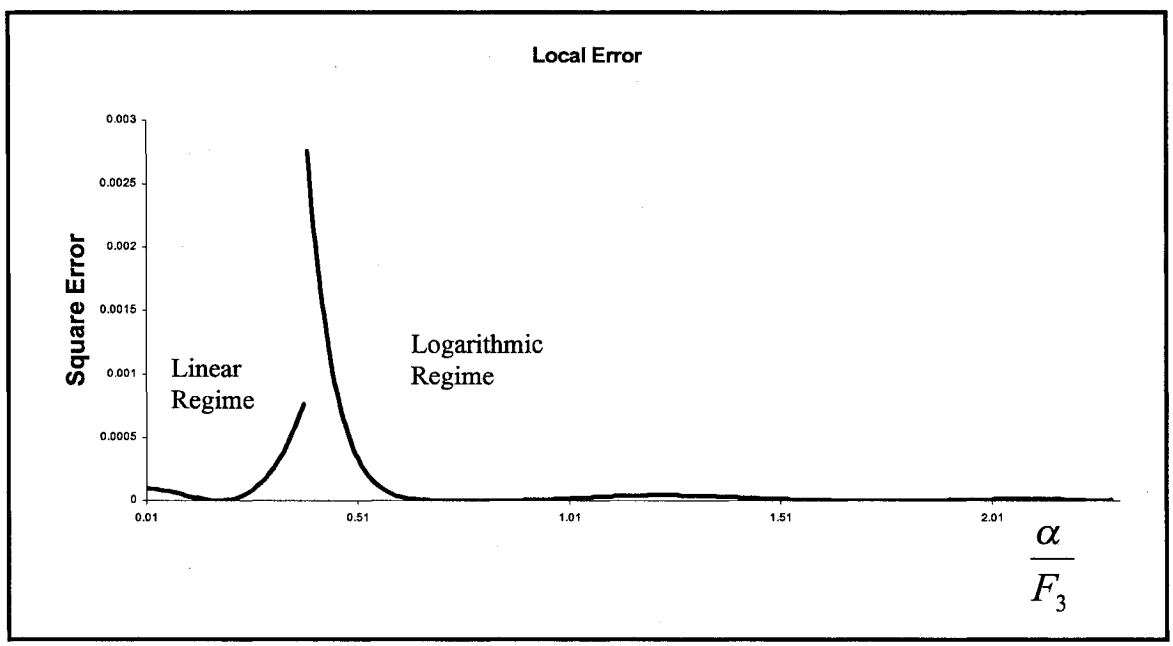

Figure 4-11: Local Error, Polynomial Function

It seems suitable at this time to present another result that was achieved during the preparation of this thesis, that is, the ability to approximate the inner and overlap vortex region of the Hoffman and Joubert circulation profiles with the use of the Vatistas n profile [22] [23]. The task is to determine the value of n that yields a good approximation to both regions, namely the region of solid body rotation and the that for the logarithmic region.

The logarithmic region of the profile has the following form and universal constant.

$$\Gamma/\Gamma_c = 2.14\log\left(r/r_c\right)+1 \quad \text{or} \quad v_\theta/v_{\theta,c} = \left(r/r_c\right)^{-1}\left(2.14\log\left(r/r_c\right)+1\right)$$

experimental results will, with a good level of accuracy, adhere to this law in the range of, say, $0.5 < r/r_c < 2.5$.

The inner region of the Hoffman and Joubert profile has the following form and universal constants,

$$\Gamma/\Gamma_c = 1.83\left(r/r_c\right)^2 \text{ or } v_\theta/v_{\theta,c} = 1.83\left(r/r_c\right)$$

in the range of, say, $0 < r/r_c < 0.5$

The Vatistas model has the form, when non-dimensionalized with core values

$$v_\theta/v_{\theta,c} = (2)^{1/n}\frac{r/r_c}{\left(1+\left(r/r_c\right)^{2n}\right)^{1/n}}$$

or,

$$\Gamma/\Gamma_c = (2)^{1/n} \frac{\left(r/r_c\right)^2}{\left(1+\left(r/r_c\right)^{2n}\right)^{1/n}}$$

it is simply a matter of matching the inner region to the Vatistas model to yield,

$$n = \ln(2)/\ln(1.83) = 1.146$$

When this function is plotted along with the universal profiles of Hoffman and Joubert it is observed that both universal inner and universal overlap regions are adequately approximated by one expression, this particular value of parameter n was able to approximate both universal constants.

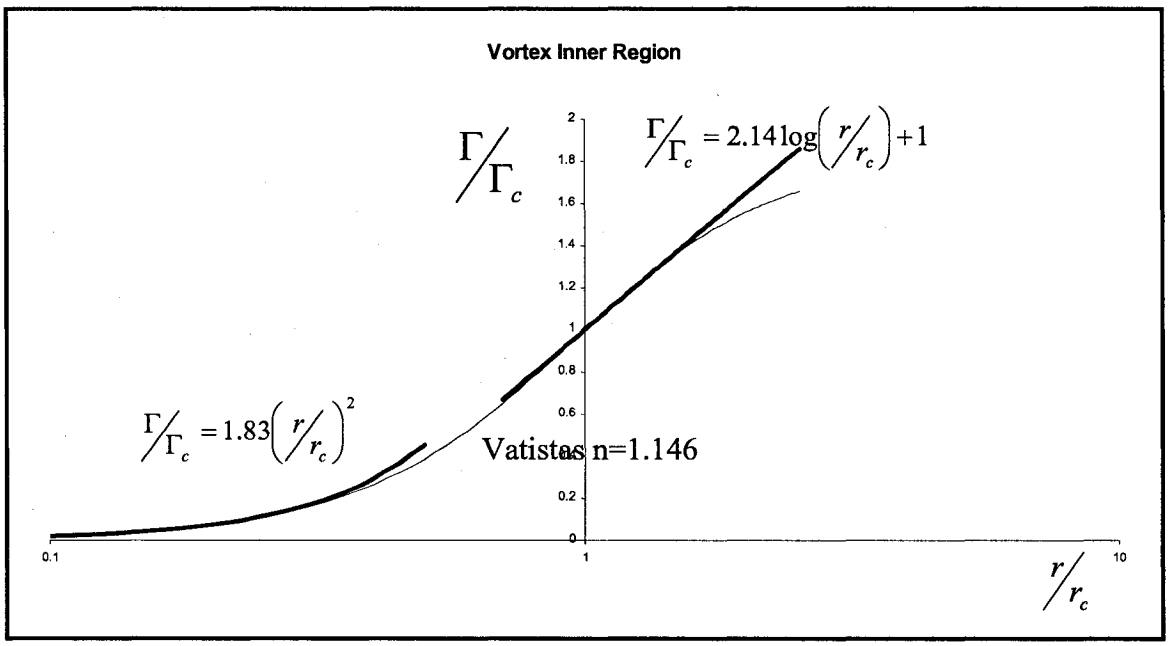

Figure 4-12: Vatistas, Circulation Profile, Semilog Scale

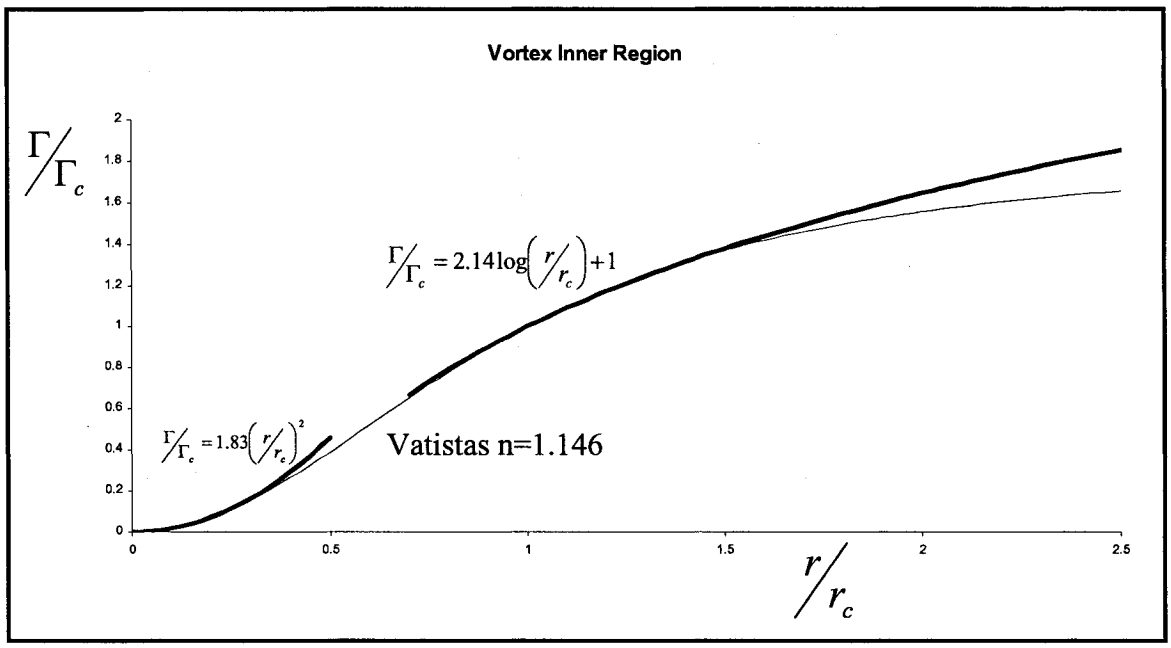

Figure 4-13: Vatistas Circulation Profile

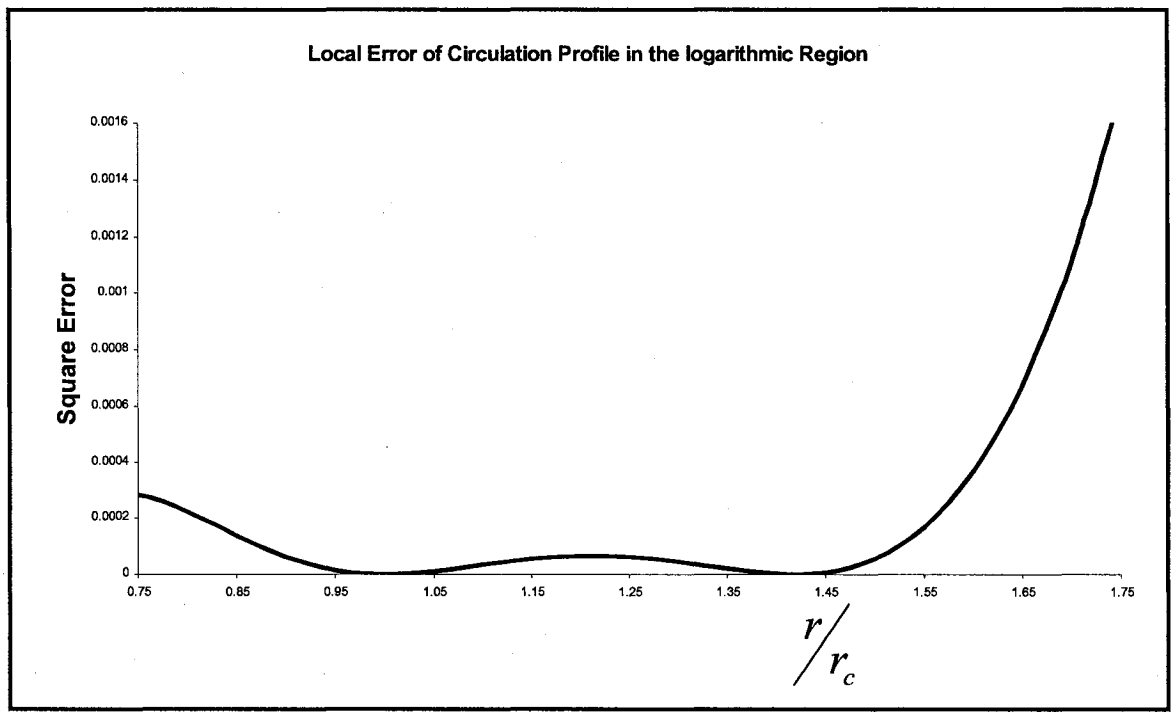

Figure 4-14: Local Error, Vatistas Circulation Profile

As we can see, in Figure 4-12, Figure 4-13 and Figure 4-14 the agreement is very good until about $r/r_c = 1.75$. Also, as with any idealized vortex model, the core circulation is a fixed fraction of the total circulation. This property is in disagreement with the outer defect law of Hoffman and Joubert, which states that the outer law is not universal and is observed to be a function of the outer variables. However, what we do observe is that, for the Vatistas model,

$$\Gamma_0/\Gamma_c = (2)^{1/1.146} = 1.83 \text{ or } \Gamma_c/\Gamma_0 = 0.546$$

So that 54.6% of the circulation is rolled up into the core. Again, this is a good representation of the results obtained in the experiments. This justifies the use of $n = 1.146$ as a suitable idealized vortex for the purposes of modeling the characteristics of the trailing tip vortex.

Since the outer component of the profile is of limited use it serves us to approximate the Vatistas profile with a precise polynomial fit of low order. This simple approach achieves this. First the denominator is expanded, about the core radius, and terms of order greater than two are disregarded,

$$(2)^{1/n}\frac{1}{\left(1+\left(r/r_c\right)^{2n}\right)^{1/n}} = 1-\left(\left(r/r_c\right)-1\right)+\left(1-\frac{n}{2}\right)\left(\left(r/r_c\right)-1\right)^2+O^3$$

Second, this expression is multiplied by the numerator to yield the final expression.

$$\boxed{\frac{\Gamma}{\Gamma_c} \cong \left(r/r_c\right)^2\left(3+\left(r/r_c\right)\left(\left(r/r_c\right)-3\right)-\frac{n}{2}\left(\left(r/r_c\right)-1\right)^2\right)}$$

This yields a very good approximation over the entire Inner region and Logarithmic region (see Figure 4-15 and Figure 4-16)

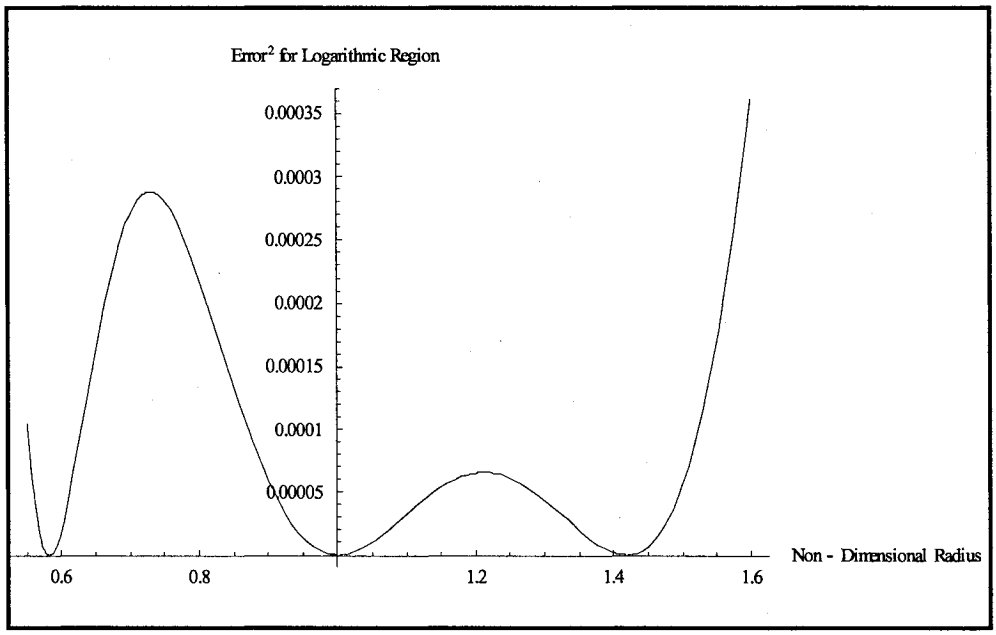

Figure 4-15: Local Error over Logarithmic Region, Vatistas Circulation Profile, Finite Expansion

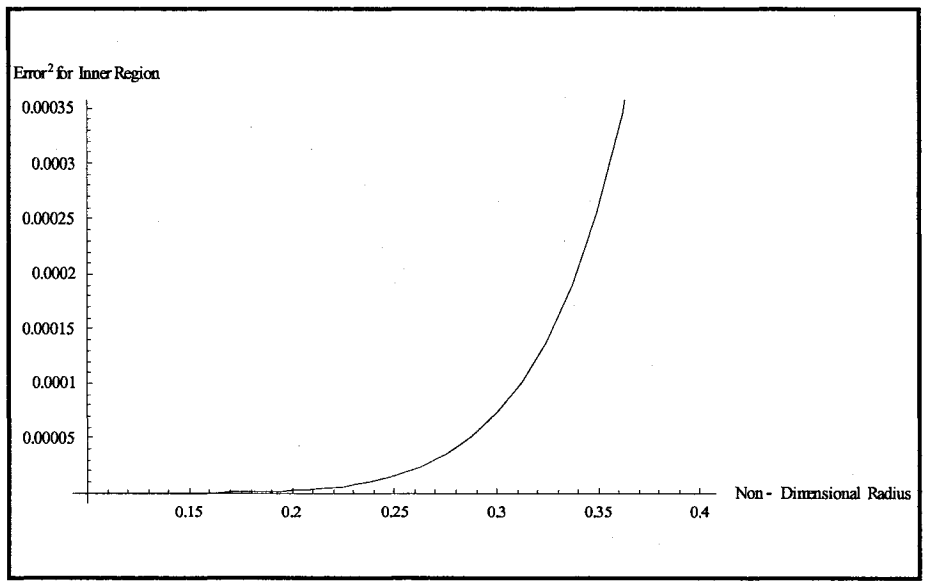

Figure 4-16: Local Error over Inner Region, Vatistas Circulation Profile, Finite Expansion

4.5 Tip Vortex Intensity

The general circulation at a given radial location is calculated as,

$$\Gamma = \int_0^{2\pi} U_\infty \alpha^* \cdot G\left(\frac{r}{r_c}\right) \cdot r d\theta = 2\pi \cdot U_\infty \alpha^* G\left(\frac{r}{r_c}\right) \cdot r$$

The logarithmic velocity variation can be used to calculate the circulation,

$$\Gamma = 2\pi \cdot U_\infty \left(K \ln\left(\alpha_E / F_3\right) + B \right) G\left(\frac{r}{r_c}\right) \cdot r$$

Or we may use the general polynomial expression for the velocity profile to obtain an expression for the circulation on the Far Field and Intermediate Field regimes,

$$\Gamma = 2\pi \cdot U_\infty \sum_{i=1}^{N} a_i \left(\frac{\alpha}{F_3}\right)^i G\left(\frac{r}{r_c}\right) \cdot r$$

Now we can evaluate the circulation at any multiple of the core radius, $r = k \cdot r_c$

$$\Gamma_{\frac{r}{r_c}=a} = 2\pi \cdot U_\infty \alpha^* G(k) \cdot k \cdot r_c$$

It is interesting to evaluate this function far away from the origin where the profile attains the potential vortex profile. This can be done assuming the self-similarity of the profile extends to the outer region (which is admittedly just approximate) such that,

$$G(k) = G\left(\frac{r}{r_c}\right)\Big|_{r=kr_c} = 1 \Big/ \left(\frac{r}{r_c}\right)\Big|_{r=kr_c} = \left(\frac{1}{k}\right)$$

therefore,

$$\Gamma_0 = 2\pi \cdot U_\infty \alpha^* \, 1/k \cdot k \cdot r_c$$

$$\boxed{\frac{\Gamma_0}{2\pi \cdot U_\infty r_c} = \alpha^*} \quad (5a)$$

$$\boxed{\frac{\Gamma_0}{2\pi \cdot U_\infty r_c} = \sum_{i=1}^{N} a_i \left(\alpha_E / F_3 \right)^i} \quad (5b)$$

or strictly in the Intermediate field regime,

$$\boxed{\frac{\Gamma_0}{2\pi \cdot U_\infty r_c} = K \ln\left(\alpha_E / F_3 \right) + B} \quad (5c)$$

We see that the same proportionality constant that scales the maximum velocity scales the dimensionless vortex intensity. If the left hand side were plotted for a given wing, Reynolds Number, and Streamwise location, the same varition with angle of attack should be obtained as the one which was obtained with the tangential velocity. Fortunately such data can be found, see Figure 4-17 and Figure 4-18, and its presence serves not only to validate equation (4) but equation (5) as well (see figure below).

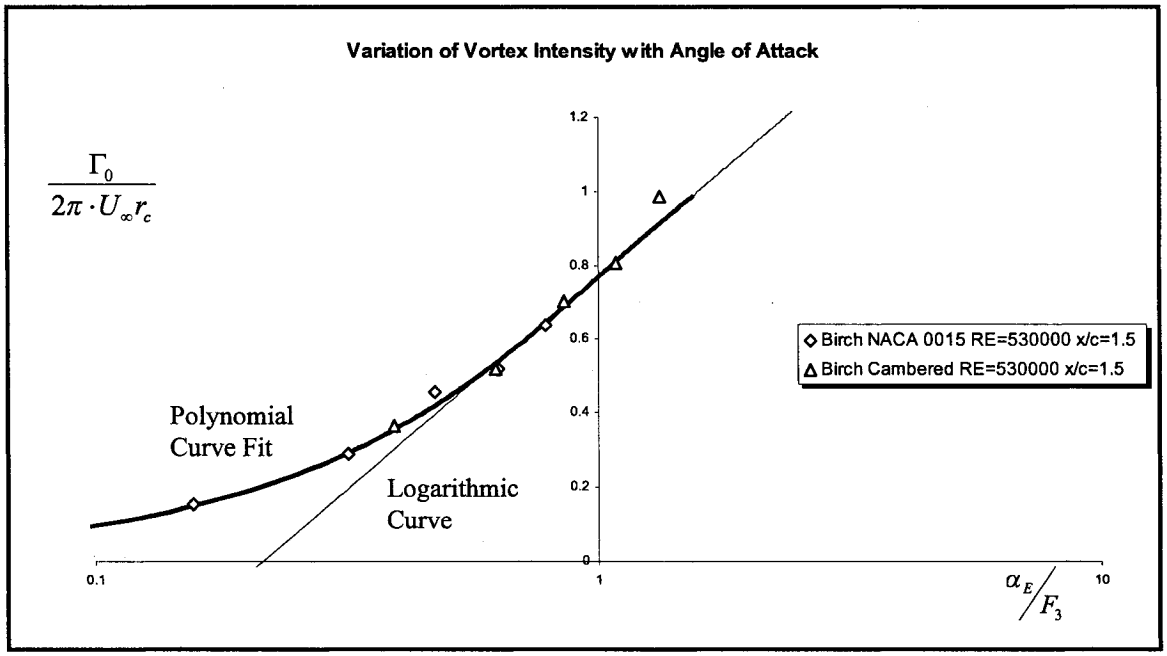

Figure 4-17: Variation of Vortex Intensity with Angle of Attack, Semilog Scale

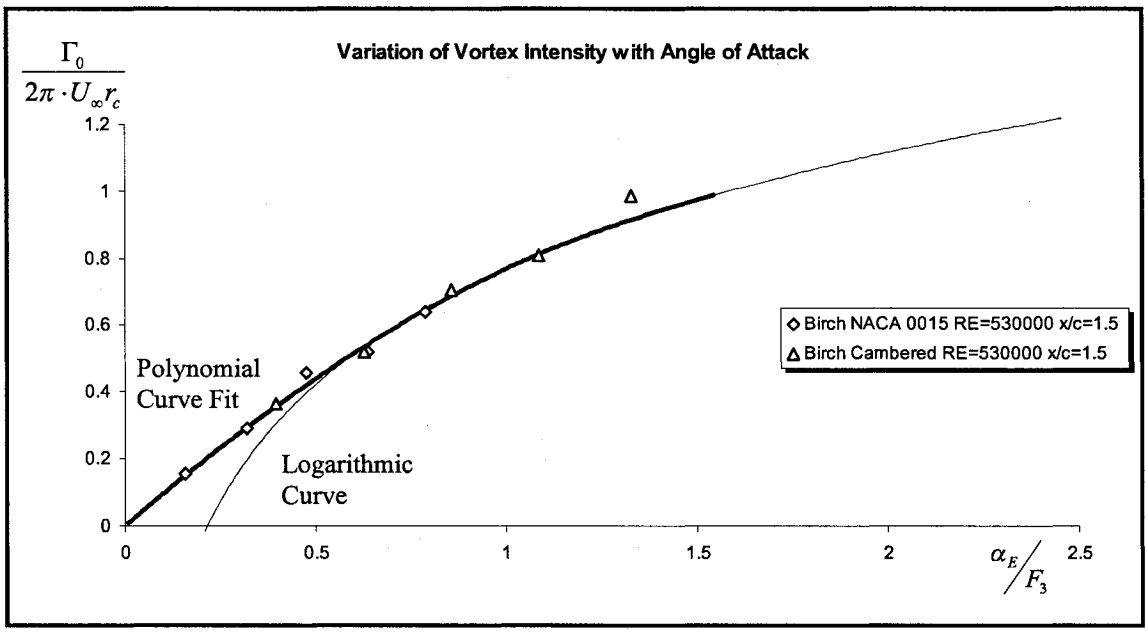

Figure 4-18: Variation of Vortex Intensity with Angle of Attack

We may also use the expression for the circulation to gain a useful observation about the model which we have chosen to use. We can use the expression in (5) to non-dimensionalize the circulation. To do this we divide the circulation by (5) to yield,

$$\Gamma/\Gamma_0 = G\left(r/r_c\right)\cdot r/r_c$$

Which shows that our results are indeed consistent with that of an idealized vortex model. Also we observe that,

$$\Gamma_c/\Gamma_0 = G(1)$$

This value was obtained in curve fitting the maximum velocity in equation (4). As a result of this we may write an expression for the maximum velocity as,

$$\boxed{\frac{v_{\theta,\max}}{U_\infty} = \left(\Gamma_c/\Gamma_0\right)\alpha^*}$$

If we decided to use the $n = 1.146$ vortex model for the calculation of $\left(\Gamma_c/\Gamma_0\right)$ this would yield,

$$\frac{v_{\theta,\max}}{U_\infty} = 0.546\sum_{i=1}^{N} a_i\left(\frac{\alpha_E}{F_3}\right)^i$$

over the logarithmic regime,

$$\frac{v_{\theta,\max}}{U_\infty} = 0.546\left(K\ln\left(\alpha_E/F_3\right)+B\right)$$

The effect of this is to obtain a very simple model which only requires the curve fitting of one variable, namely, F_3.

4.6 Axial Velocity

Batchelors analysis [19] of axial flow in a trailing vortex is still used to this day (see Spalart [29] or Anderson and Lawton [3]) the model can display velocity excess or deficit (which is only attributed to boundary layer friction on the tip) yet has no explicit mechanism to explain the effect of angle of attack which has been displayed.

His model uses Bernoulli's equation with losses *along a streamline*,

$$\frac{P_\infty}{\rho}+\frac{U_\infty{}^2}{2}+\Delta H=\frac{p}{\rho}+\frac{(u^2+v_\theta{}^2)}{2}$$

And the Radial Momentum for axisymmetric vortex flow,

$$\frac{P_o-p}{\rho}=\int_r^\infty\frac{v_\theta{}^2}{r}dr$$

The final assumption made by Bachelor is that the far pressure boundary, perpendicular to the vortex line, is equal to the free stream value,

$$P_o=P_\infty$$

Noting that, for axisymetric swirling flows,

$$\Gamma(r)=v_\theta r2\pi$$

$$u^2=U_\infty{}^2+\int_r^\infty\frac{1}{(2\pi r)^2}\frac{\partial(\Gamma^2)}{\partial r}dr-2\Delta H$$

The second term on the right hand side represents the increase in axial velocity due to the swirling of the flow whereas the third term represents the decrease in axial velocity due to friction.

Although his analysis may contain valid assumptions when off the wing, when on the wing, a better approximation is that the wing itself imposes the perpendicular "far" pressure, i.e.

$$P_o = P_{upper} = C_{pu}\frac{1}{2}\rho U_\infty{}^2 + P_\infty$$

This gives the modified results,

$$u^2 = U_\infty{}^2 + \int_r^\infty \frac{1}{(2\pi r)^2}\frac{\partial(\Gamma^2)}{\partial r}dr - (2\Delta H + C_{pu}U_\infty{}^2) \quad (6)$$

The addition of the last term on the right takes into account a further increase in axial velocity due to the lower pressure imposed by the wing.

It is also of interest to note that if there is no swirl ($\Gamma = 0$) or losses ($\Delta H = 0$), our expression becomes the conventional expression for the coefficient of pressure,

$$C_{pu} = 1 - u^2 / U_\infty{}^2$$

Additionally, if we are not on the wing the coefficient of pressure is zero and we revert be to Bachelors expression.

This expression can be put into a more convenient form by inserting the expression for the circulation which we obtained previously.

$$\Gamma = \Gamma_0 G\left(\frac{r}{r_c}\right)\frac{r}{r_c} = \alpha^* 2\pi \cdot U_\infty G\left(\frac{r}{r_c}\right) r$$

$$\int_r^\infty \frac{1}{(2\pi r)^2}\frac{d(\Gamma^2)}{dr}dr = (U_\infty \alpha^*)^2 \cdot \int_r^\infty \frac{1}{r^2}\frac{d}{dr}\left(G\left(\frac{r}{r_c}\right)r\right)^2 dr$$

Then performing the following transformation

$$r^* = \frac{r}{r_c}$$
$$r_c dr^* = dr$$

Immediately, a relationship is obtained,

$$\boxed{\left(\frac{u}{U_\infty}\right)^2 = (1 - \frac{\Delta P_t}{\frac{1}{2}\rho U_\infty{}^2} - C_{pu}) + V \cdot \alpha^{*2}}$$

Where,

$$V = \int_{r^*}^\infty {}^1\!/_{r^{*2}} \frac{d}{dr^*}\left(G(r^*)r^*\right)^2 dr^*$$

If in the Intermediate Field regime then

$$\boxed{\left(\frac{u}{U_\infty}\right)^2 = (1 - \frac{\Delta P_t}{\frac{1}{2}\rho U_\infty{}^2} - C_{pu}) + V \cdot \left(K \ln\left({}^{\alpha_E}\!/_{F_3}\right) + B\right)^2}$$

Or using the polynomial to approximate the entire Far to Intermediate regime,

$$\boxed{\left(\frac{u}{U_\infty}\right)^2 = (1 - \frac{\Delta P_t}{\frac{1}{2}\rho U_\infty{}^2} - C_{pu}) + V \cdot \left(\sum_{i=1}^N a_i \left({}^{\alpha_E}\!/_{F_3}\right)\right)^2}$$

Let's take the analysis further by placing some simple algebraic vortex models into the equation; for example,

the $n = 2$ model would yield,

$$V = \left(\frac{\pi}{2} - \frac{r^{*2}}{1 + r^{*4}} - \text{atan}\left(r^{*2}\right) \right)$$

the *Lamb* model would yield,

$$V = 2\int_{t=1}^{\infty} \frac{e^{-r^{*2}t} - e^{-2r^{*2}t}}{t} dt$$

Lets note that the value of the function V is comparable to (but not equal to) the loss-less profile, as can be seen in the plot of Figure 4-19, corresponding to the *Lamb* model and the $n = 2$ model.

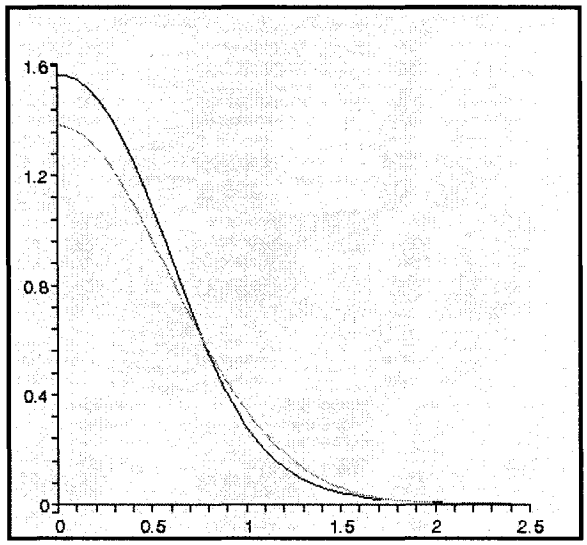

Figure 4-19: Variation of V with Radius, (the function with the higher peak is the Vatistas model and the other is the Lamb)

From thin airfoil theory (i.e. for a flat plate at low angle of attack),

$$C_{pu} = -\left(\frac{A^2 \alpha_E{}^2}{4} + A\alpha_E \right)$$

Where, $A = \frac{c-x}{\sqrt{cx-x^2}}$

Characteristic measurements of the axial velocity are typically taken at the centerline. Therefore it is useful to evaluate the expression at the centerline. Doing this gives the expression,

$$\left(\frac{u_{\max}}{U_\infty}\right)^2 = \left(1 - \frac{\Delta P_t}{\frac{1}{2}\rho U_\infty{}^2}\right) + A\alpha_E + \left(\frac{A^2}{4}\right)\alpha_E{}^2 + V\left(r^* = 0\right)\cdot\alpha^{*2}$$

When we are off the wing, i.e. $C_{pu} = 0$, we revert to Bachelors equation; the final form of the expression for the centerline axial velocity, off the wing, is for example,

for the $n = 2$ Model,

$$\left(\frac{u_{\max}}{U_\infty}\right)^2 = \left(1 - \frac{\Delta P_t}{\frac{1}{2}\rho U_\infty{}^2}\right) + \frac{\pi}{2}\alpha^{*2}$$

Similarly, for the *Lamb Oseen* [24] [25] Model,

$$\left(\frac{u_{\max}}{U_\infty}\right)^2 = \left(1 - \frac{\Delta P_t}{\frac{1}{2}\rho U_\infty{}^2}\right) + 2\ln(2)\alpha^{*2}$$

It is reasonable to ask whether the values of $V\left(r^* = 0\right)$ as calculated by these idealized vortex models are representative of what may be obtained in an actual tip vortex. Or rather, how sensitive is the value of $V\left(r^* = 0\right)$ to deviations from these ideal vortex profiles. This would be useful so that if the data is curve fitted for values of $V\left(r^* = 0\right)$, we will know if the values obtained are indeed "physical". Since $V\left(r^*\right)$ is an integral, the

use of a piecewise linear profile, that is approximately characteristic of the tip vortex should serve our purposes sufficiently. First we rewrite $V(r^*)$ as,

$$V = \int_{r^*}^{\infty} 1/r^{*2} \frac{d}{dr^*}(\Gamma/\Gamma_o)^2 \cdot dr^*$$

and propose,

$$\Gamma/\Gamma_o = (\Gamma_c/\Gamma_o) A r^{*2} \text{ from } 0 < r^* < R_0$$

$$\Gamma/\Gamma_o = (\Gamma_c/\Gamma_o)(B\log(r^*)+1) \text{ from } R_0 < r^* < R_1$$

$$\Gamma/\Gamma_o = 1 \text{ for } r^* > R_1$$

We can take the transition R_0 as the location of minimum difference between the first and second region. Or where,

$$\frac{\partial}{\partial r^*}\left(Ar^{*2} - (B\log(r^*)+1)\right)\Big|_{r^*=R_o} = 0$$

Corresponding to,

$$R_0 = \left(\frac{B}{2\ln(10)}\frac{1}{A}\right)^{0.5}$$

The second radius of transition can occur at the intersection of the second and third region,

$$R_1 = 10^{\frac{1-\Gamma_c/\Gamma_0}{B(\Gamma_c/\Gamma_0)}}$$

Then evaluating V for this piece wise model yields,

$$V = (\Gamma_c/\Gamma_o)^2 \left(A^2 \int_{r^*}^{R_1} 1/r^{*2} \frac{d}{dr^*}\left(r^{*2}\right)^2 \cdot dr^* + \int_{R_1}^{R_2} 1/r^{*2} \frac{d}{dr^*}(B\log(r^*)+1)^2 \cdot dr^* \right)$$

$$V(r^* = 0) = (\Gamma_c/\Gamma_o)^2 \left(2A^2(R_0) - \frac{B\left((R_0 - R_1)(R_0 + R_1)(B + \ln(100)) - 2B\left(R_1^{\,2}\ln(R_0) + R_0^{\,2}\ln(R_1)\right)\right)}{2(R_0 R_1 \ln(10))^2} \right)$$

If we plot the value of $V(r^* = 0)$ as a function of (Γ_c/Γ_o) inserting the universal values of $A = 1.83$ and $B = 2.14$ we obtain the following plot, shown in Figure 4-20,

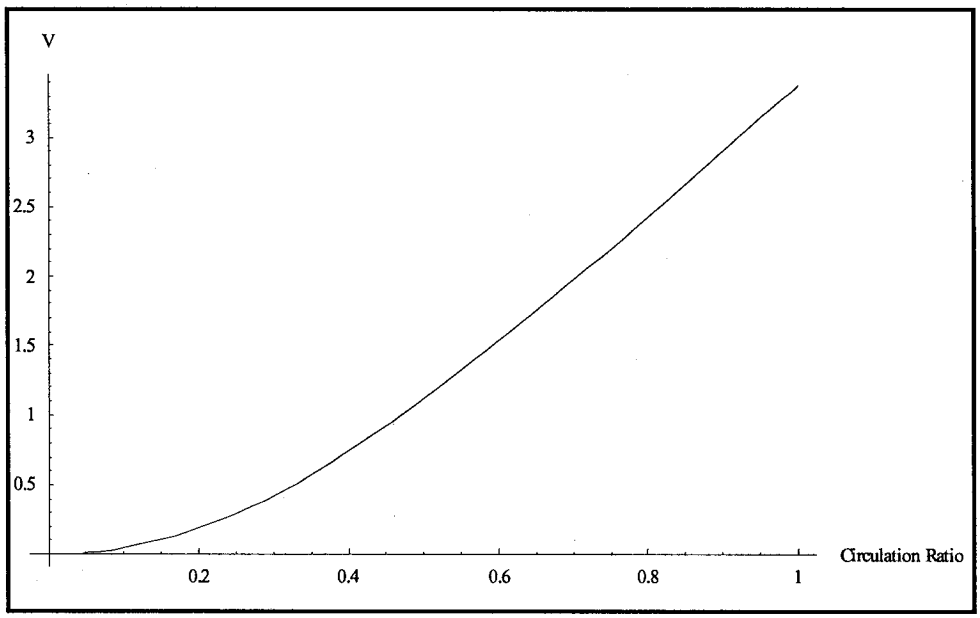

Figure 4-20: Variation of V_{max} with Circulation Ratio

Note that, $(\Gamma_c/\Gamma_o) = 1$, corresponds to the Rankine Vortex. It can now be anticipated that we expect values in that range, noting that the analysis performed was rough and is just to give us a feeling about the problem at hand.

In the restricted case, that the total pressure loss is relatively constant over a range of angles of attack it should be possible to curve fit the data to the form,

$$\left[\frac{(u_{\max}/U_\infty)^2 - K_1}{K_2}\right]^{0.5} = \alpha^*$$

Where, $K_1 = \left(1 - {\Delta P_t}/{1/2\,\rho U_\infty{}^2}\right), K_2 = V$ are curve fitted values.

Again expanding this over the appropriate regimes yields,

$$\left[\frac{(u_{\max}/U_\infty)^2 - K_1}{K_2}\right]^{0.5} = \left(K \ln\left({\alpha_E}/{F_3}\right) + B\right)$$

In the Intermediate Regime, Or

$$\left[\frac{(u_{\max}/U_\infty)^2 - K_1}{K_2}\right]^{0.5} = \left(\sum_{i=1}^{N} a_i \left({\alpha_E}/{F_3}\right)\right)$$

as a curve fit covering the entire Far Field To Intermediate Field regime.

This yields an estimate of the function $V(r^* = 0)$, as well as, total pressure loss. From Figure 4-21 and Figure 4-22, we see that this rule is observed to sometimes hold. There is difficulty in the low angle of attack region to fit the curve, surely because the total pressure loss must drop to zero as the angle of attack is decreased or as we increase distance from the wing (increasing F_3).

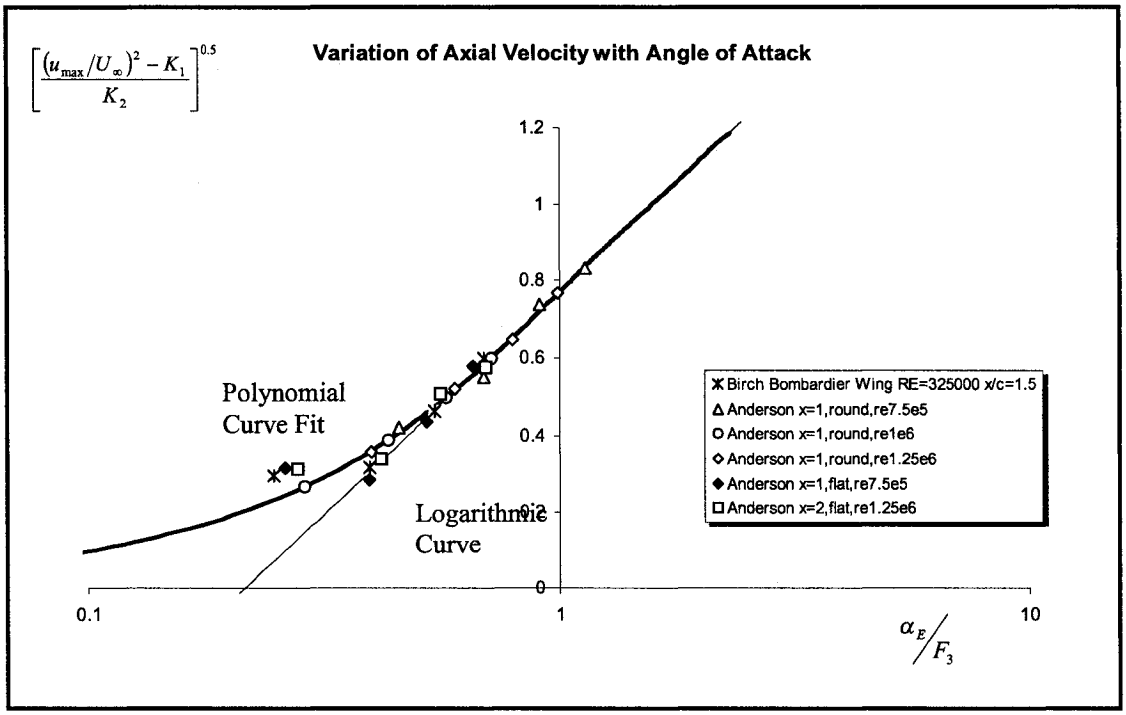

Figure 4-21: Variation of Axial Velocity with Angle of Attack, Semilog Scale

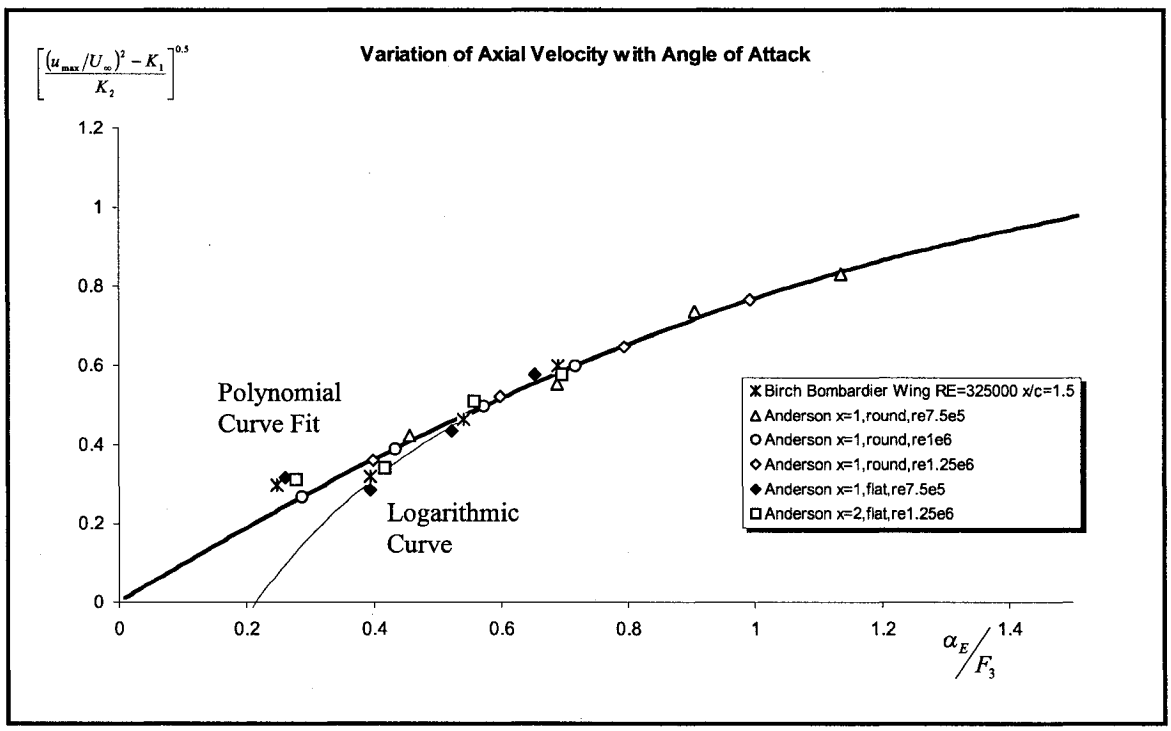

Figure 4-22: Variation of Axial Velocity with Angle of Attack

4.7 Circulation

The results of equation (5) are encouraging and helpful, however, circulation and core radius are both dependent variables and it would be more desirable to decouple this relation with the use of an auxiliary relationship.

This can be done using evidence that has shown that the tip vortex strength scales, as a fixed fraction, with a characteristic circulation bound to the wing itself, as result making it independent of angle of attack (see Desabrais and Johari [30] or Astolfi et al. [31] for data of this type). Such a characteristic circulation could be the circulation at the root section. In this analysis we will choose the characteristic circulation to be the average circulation of the wing, this can be stated as,

$$\frac{\Gamma_o}{\overline{\Gamma}_{bound}} = \gamma = fn\left(\mathrm{Re}, \frac{x}{c}\right)$$

From the Kutta-Joukoski theory,

$$\Gamma_{bound} = \tfrac{1}{2} U_\infty c C_l$$

Integrating this across the span will give us an expression for the average circulation across the section,

$$\int_{\frac{-b}{2}}^{\frac{b}{2}} \frac{\Gamma_{bound}}{b} ds = \overline{\Gamma}_{bound} = \int_{\frac{-b}{2}}^{\frac{b}{2}} \frac{U_\infty c C_l}{2b} ds = \frac{U_\infty c C_L}{2}$$

This shows equivalence between scaling with bound circulation and scaling with total lift, if independence of angle of attack was observed in the previous case, it should be observed in this case as well. This could also be expressed in the form

$$\overline{\Gamma}_{bound} = \frac{U_\infty c a \alpha_E}{2}$$

Assuming data of the type proposed, we may express the tip vortex strength as,

$$\frac{\Gamma_o}{U_\infty c} = \gamma \frac{a \alpha_E}{2}$$

Which shows that, for a given wing, there is equivalence between scaling the tip vortex circulation with bound circulation and obtaining independence of angle of attack and the total circulation of the tip vortex to be a linear function of angle of attack (see Birch [4][5], Anderson [3], or Shekarriz [6] to name a few).

We can also remark that mathematical estimates of loading at the tips of wings are usually seen to be expressible as linear functions of root circulation. If this tip loading is of the order of the tip vortex circulation and assuming that the root circulation is a linear function of angle of attack (if the wing is long enough) we are left, by dimensional reasoning, that the tip vortex circulation scales with the wing circulation. This is, essentially, the analysis used by Moore and Saffman to obtain the circulation distribution in the vortex.

We see that all these statements are totally equivalent, based on what has been observed, in summary we may say that the tip vortex strength at given Reynolds number and Streamwise location is a linear function of Angle of Attack,

$$\boxed{\frac{\Gamma_o}{U_\infty c} = \kappa \alpha_E \qquad \kappa = \gamma \frac{d\bar{\Gamma}_{bound}}{d\alpha}} \quad (6)$$

this value of κ can be either measured directly (see Figure 4-23, the value of κ to be used in subsequent calculations are the slopes of the lines shown in the table), or the value of the bound circulation may be approximated using whatever method is desired (one example being the relations presented above) with the value of γ being estimated as best as possible; the value of γ has been quoted as ranging between 66-80 percent. Let us make the observation that there is nothing wrong (although probably not very common) that this value exceeds 1 since we are dealing with the average bound circulation, as opposed to the root circulation.

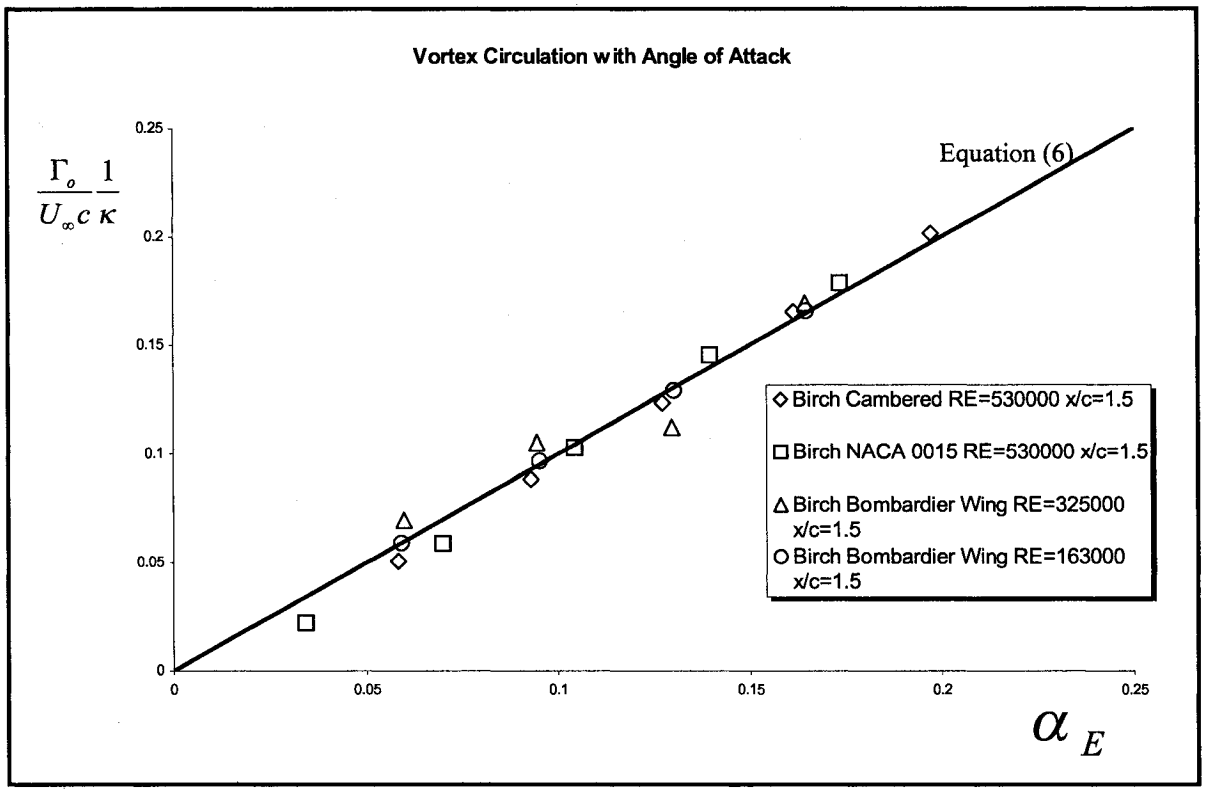

Figure 4-23: Variation of Tip Vortex Circulation with Angle of Attack

Two additional points could be made about κ. First, κ has often been shown not to be a strong function of Reynolds number (see Anderson or Desabrais for examples of this), however, for purposes of generality we shall leave it as one. Second, κ will no longer be a function of streamwise position once roll-up completes, this being due to the fact that the divergence of vorticity is always zero, or equivalently, circulation is constant along a vortex tube. This is a kinematic property, independent of the flow conditions. Once decay ensues the circulation of the vortex does not decrease, the vortex simply grows, diffusing its vorticity. For this reason κ is constant after roll-up.

Displayed in Table 8 is the value of κ as obtained for the data displayed in the figure. These values will be used in subsequent calculations.

Table 8: Rate of Change of Tip Vortex Circulation with Angle of Attack

	κ
Birch Bombardier Wing RE=163000 x/c=1.5	2.1
Birch Bombardier Wing RE=325000 x/c=1.5	1.541
Birch NACA 0015 RE=530000 x/c=1.5	1.354
Birch Cambered RE=530000 x/c=1.5	1.75

4.8 Core Radius

Going back to equation (5) and inserting (6) we can obtain a simple expression for the variation of the core radius with angle of attack,

$$\frac{r_c}{c} = \kappa F_3 / 2\pi \; \frac{\alpha_E / F_3}{\alpha^*} \quad (7a)$$

in the Logarithmic regime,

$$\frac{r_c}{c} = \kappa F_3 / 2\pi \; \frac{\alpha_E / F_3}{\left(K \ln\left(\alpha_E / F_3 \right) + B \right)} \quad (7c)$$

or over both the Far Field and Logarithm Field regimes,

$$\frac{r_c}{c} = \kappa F_3 / 2\pi \; \frac{\alpha_E / F_3}{\sum_{i}^{N} a_i \left(\alpha_E / F_3 \right)^i} \quad (7b)$$

Using the value of κ as calculated by the tip vortex circulation section and the value of the function F_3, as obtained in the curve fitting of the core velocity, we obtain the following predictions (Figure 4-24 and Figure 4-25) for the value of core radius.

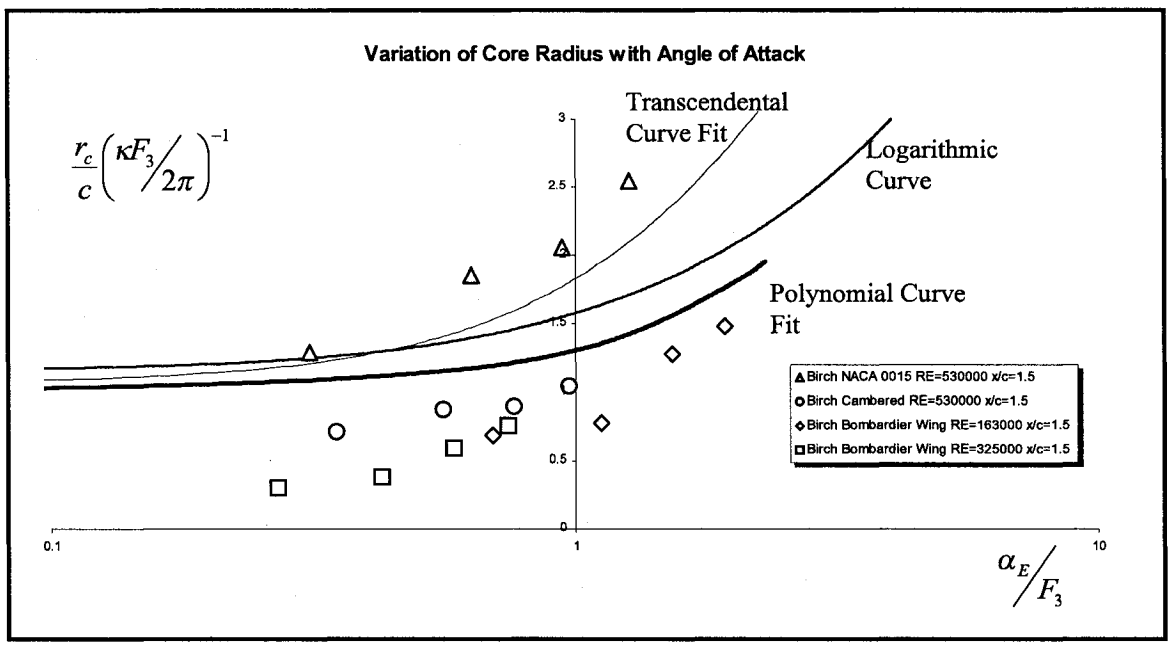

Figure 4-24: Variation of Core Radius With Angle of Attack, Semilog Scale

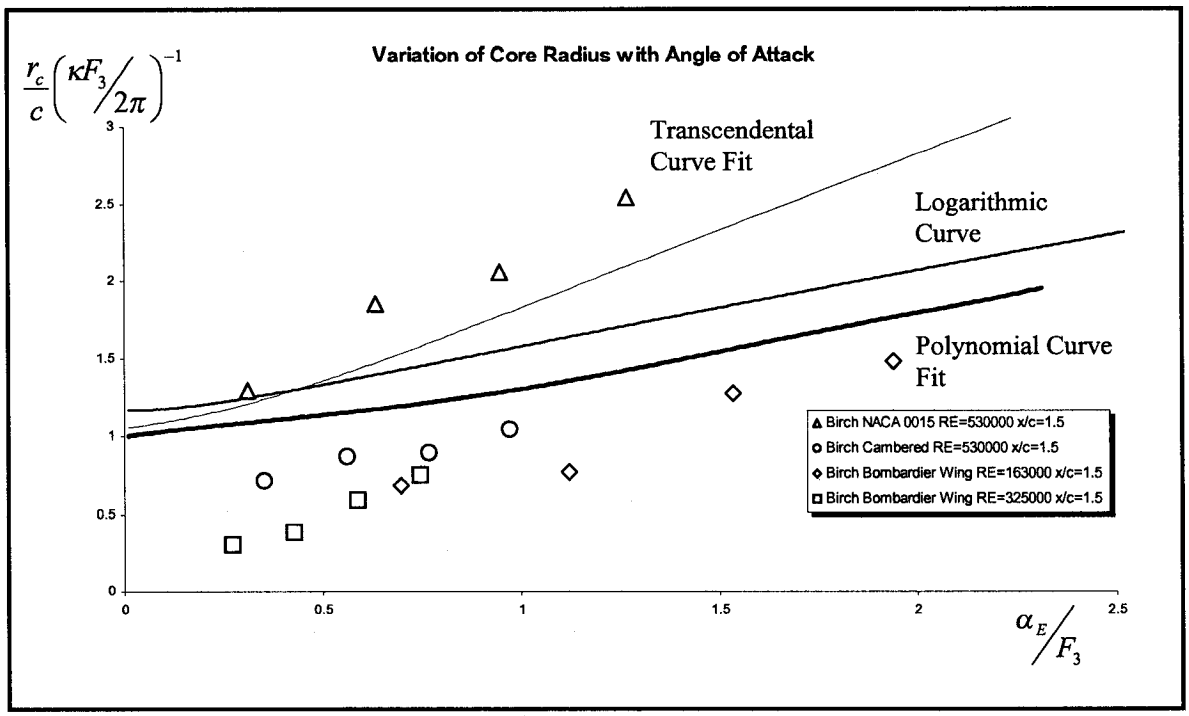

Figure 4-25: Variation of Core Radius With Angle of Attack

The three curves correspond, from bottom to top to, that calculated from the polynomial expression, the purely logarithmic curve, and thirdly the core radius was calculated from the transcendental curve fit that was proposed. It is seen that even though these curves were able to approximate each other with little error, they vary appreciably when used to calculate the core radius. Although the numerical values corresponding to the measured core radius do not correspond to that which are predicted, the order of magnitude is predicted and the trend of increasing core radius with angle of attack is explained. Also, this result presents an improvement from Moore and Saffman with respect to the dependence of the core radius with angle of attack, their theory predicts that the core radius is independent of angle of attack. It can be seen that their solution is asymptotically attained as the angle of attack is decreased.

5 Concluding Remarks

The thesis investigated the fundamental properties of Tip Vortex flows. It conducted this study from the Near to Far Field and, in the process defined an Intermediate Field.

It used FLUENT in its Viscous Incompressible simulation of a finite wing with a constant NACA 0012 airfoil cross section. The Spalart-Allmaras Turbulence Model combined with Wall Functions was selected and was shown to yield reasonable results. When compared with, a simple, Prandl Lifting Line Theory and airfoil section data Lift Coefficient, for the finite wing, was predicted within 10.1% and Drag Coefficient was predicted within 10.7% . Also, wing loading distribution is very well predicted.

The Tip Vortex, in the Near Field obtained in the simulation, is observed to adhere to Hoffman and Jouberts universal circulation profile [13] and vorticity contours compare to those obtained by in [5]. The development of the Tip Vortex is described; the tip vortex generated has tangential velocities on the order of half the free stream value and it is observed that it initiates with two vortices forming very near the Leading Edge like those of [2], [8], [9] and [18] to name a few. There are total pressure losses because the fluid composing the tip vortex has been in the boundary layer and these losses affect the axial velocity. The axial velocity gradient is large and comparable to those found in [3], [4], [5] and [26]. Also, shear stress on the wing was useful in tracking the trajectory of the vortex.

The thesis included an analysis that helps explain the dependence of the Tip Vortex characteristics and their variation with angle of attack and downstream distance. The, low wing loading, analysis of Moore and Saffman [20] is used as the asymptotic Far Field Regime. Dimensional analysis presents reasoning for a hypothetical Near Field. A balance of these two scaling laws is made and is shown to apply in an Intermediate Field Regime. In the Intermediate Field, various vortex characteristics are shown to vary as a logarithmic variation with angle of attack. The expressions obtained are shown to hold well for the peak tangential velocity. Once the approximation of universality of the external profile is assumed, an expression coupling the circulation and the core radius is obtained. This is used to obtain an expression for the axial velocity; under the assumption of constant total pressure losses over a range of angles of attack, the expression obtained is shown to be in agreement with experimental data, under this restricted case. Also, the Core Radius is decoupled with the use of an auxiliary relationship for the Total Circulation that assumes, justifiably, that it scales linearly with angle of attack. The resulting expression for Core Radius is in qualitative agreement with experiment.

6 References

[1] Spalart, P.R., Allmaras, S.R., "A One-Equation Turbulence Model for Aerodynamic Flows," *Technical Report AIAA-92-0439*, AIAA, 1992.

[2] Dacles-Mariani, J., Zilliac, G., Chow, J.S., Bradshaw, P. "Numerical/Experimental Study of a Wingtip Vortex in the Near Field," *AIAA Journal*, Vol. 33, No. 9, September 1995, pp. 1561-1568.

[3] Anderson, E.A., Lawton, T.A., "Correlation Between Vortex Strength and Axial Velocity in a Trailing Vortex," *J. Aircraft*, Vol. 40, No. 4, July-August 2003, pp. 699-704.

[4] Birch, D., Lee, T., Mokhtarian, F., Kafyeke, F., "Rollup and Near-Field Behavior of a Tip Vortex," *J. Aircraft*, Vol. 40, No. 3, 2003, pp. 603-607.

[5] Birch, D., Lee, T., Mokhtarian, F., Kafyeke, F., "Structure and Induced Drag of a Tip Vortex," *J. Aircraft*, Vol. 41, No. 5, September-October 2004, pp. 1138-1145.

[6] Shekarriz, A., Fu, T.C., Katz, J., Huang, T.T., "Near-Field Behavior of a Tip Vortex," *AIAA Journal*, Vol. 31, No. 1, January 1993, pp. 112-118.

[7] Dacles-Mariani, J., Kwak, D., Zilliac, G., "On Numerical Errors and Turbulence Modeling in Tip Vortex Flow Prediction," *Int. J. Numer. Meth. Fluids*, Vol. 30, 1999, pp. 65-82.

[8] Chow, J.S., Zilliac, G.G., Bradshaw, P., "Mean and Turbulence Measurements in the Near Field of a Wingtip Vortex," *AIAA Journal*, Vol. 35, No. 10, October 1997, pp. 1561-1567.

[9] Fleig, O., Arakawa C., "Large Eddy Simulation of Tip Vortex Flow at High Reynolds Number" *AIAA-2004-261*, 42nd AIAA Aerospace Sciences Meeting and Exhibit, January 2004

[10] Ghias, R., Mittal, R., Haibo, D., Lund, T.S., "Study of Tip-Vortex Formation using Large Eddy Simulation," *AIAA-2005-1280*, 43rd Fluid Dynamics Conference and Exhibit, January 2005

[11] Abott, I.H., Von Doenhoff, A.E., Stivers, L.S. Jr., "Summary of Airfoil Data," NACA Rep. 824, 1945

[12] Bertin, J.J., *Aerodynamics For Engineers*, 4th ed., Prentice Hall, New Jersey, 2002, Chap. 7.

[13] Hoffman, E.R., Joubert, P.N., "Turbulent Line Vortices," *J. Fluid Mech.*, Vol. 16, Pt. 3, 1963, pp. 395-411.

[14] Phillips, W.R.C., "The Turbulent Trailing Vortex during Roll-Up," *J. Fluid Mech.*, Vol. 105, 1981, pp. 451-467.

[15] Newman, B.G., "Flow in a Viscous Trailing Vortex," *Aeronautical Quarterly*, Vol. X, 1959, pp. 149-162

[16] Betz, A., "Behavior of Vortex Systems," *NACA Tech. Note* 713, 1933, pp. 237-253.

[17] Rossow, V.J., "Lift Generated Vortex Wakes of Subsonic Transport Aircraft," *Progress in Aerospace Science*, Vol. 35, 1999, pp. 507-660

[18] Francis, M.S., Kennedy, D.A., "Formation of a Trailing Vortex," *J. Aircraft*, Vol. 16, No. 3, March 1979, pp. 148-154.

[19] Batchelor, B. K., "Axial Flow in Trailing Vortices," *J. Fluid Mech.*, Vol. 20, Pt. 4, 1964, pp. 645-658.

[20] Moore, D.W., Saffman, P.G., "Axial Flow in Laminar Trailing Vortices," *Proc. R. Soc. Lond. A.*, Vol. 333, 1973, pp. 491-508

[21] Baker, G.R., Barker, S.J., Bofah, K.K., Saffman, P.G., "Laser Anemometer Measurments of Trailing Vortices in Water," *J. Fluid Mech.*, Vol. 65, Pt 2, 1974, pp. 325-336.

[22] Vatistas, G.H., Kozel, V., Minh, W., "A Simpler Model for Concentrated Vortices," *Exp. Fluids*, Vol. 11, 1991, pp. 73-76.

[23] Vatistas G.H., "New Model for Intense Self-Similar Vortices," AIAA Journal of Propulsion and Power, Vol. 14, No. 4, 1998, pp.462-469

[24] Lamb, H., *Hydrodynamics*, Cambridge University Press, 1932, Cambridge, UK.

[25] Oseen, C.W. "Uber Wirbelbewegune in Einer Reiben-Den Fluissikeit," *Ark. J. Mat. Astrom. Fys.* Vol. 7, pp 14-21.

[26] Devenport, W.J., Rife, M.C., Liapis, S.I., "Structure and Development of a Wing-Tip Vortex," *J. Fluid Mech.*, Vol. 312, 1996, pp. 67-106.

[27] Higuchi, H., Quadrelli, J.C., Farell, C., "Vortex Roll-Up from an Elliptic Wing at Moderately Low Reynolds Numbers," *AIAA Journal*, Vol. 25, No. 12, December 1987, pp. 1537-1542.

[28] El-Ramly, Z., Rainbird, W. J., "Flow Survey of the Vortex Wake behind Wings," *J. Aircraft*, Vol. 14, No. 11, November 1977, pp. 1102-1108.

[29] Spalart, P.R., "Airplane Trailing Vortices," *Annu. Rev. Fluid Mech.* Vol. 30, 1998, pp. 107-138.

[30] Desabrais, K.J., Johari, H., "Direct Circulation Measurments of a Tip Vortex," *AIAA Journal*, Vol. 38, No. 11, 2000, pp. 2189-2191.

[31] Astolfi, J.A., Fruman, D.H., Billard, J.Y., "A Model for Tip Vortex Roll-Up in the Near Field Region of Three-Dimensional Foils and the Predition of Cavitation Onset," *Eur. J. Mech. B/Fluids*, Vol. 18, 1999, pp. 757-775

[32] Yeung, A.F.K., Lee, B.H.K., "Particle Image Velocimetry Study of Wing-Tip Vortices," *J. Aircraft*, Vol. 36, No. 2, 1999, pp. 482-484.

[33] Panton, R.L., Oberkampf, W.L., Soskic, N., "Flight Measurments of a Wing Tip Vortex," *J. Aircraft*, Vol. 17, No. 4, April 1980, pp. 250-259.

[34] Corsiglia, V.R., Schwind, R.G., Chigier, N.A., "Rapid Scanning, Three-Dimensional Hot-Wire Anemometer Surveys of Wing-Tip Vortices" *J. Aircraft*, Vol. 10, No. 12, December 1973, pp. 752-757

[35] Wendt, B.J., "Parametric Study of Vortices Shed from Airfoil Vortex Generators," *AIAA Journal*, Vol. 42, No. 11, November 2004, pp. 2185-2195.